REFLECT DELIVERABLE D1.4

Silica Dissolution and Precipitation

Summary:

We provide new thermodynamic and kinetic data concerning the dissolution and precipitation of silica in hot and superhot geothermal systems. Different methods were applied, including traditional photometric methods and *in situ* Raman and conductimetric methods. The studies covered the interactions of silica with both pure water and saline solutions. The kinetics of silica polymerisation were studied in the presence of various metal ions and at different pH values, informed by an analysis of real geothermal water samples from the Tuzla region of Türkiye.

Authors:

Matthew Vosper, British Geological Survey, UK, Geochemist
Juliane Kummerow, Helmholtz Centre Potsdam – GFZ German Research Centre for Geosciences, Germany, Research Associate
Mustafa Demir, İzmir Institute of Technology, Türkiye, Dean of Engineering Faculty
Morten Tjelta, Institute for Energy Technology, Norway, Research Scientist

This project has received funding from the European Union's Horizon 2020 research and innovation programme under grant agreement nº 850626.

Title:	Report on silica dissolution and precipitation kinetics
Lead beneficiary:	UKRI BGS
Other beneficiaries:	GFZ, IZTECH, IFE
Due date:	30.09.2023
Nature:	Public
Diffusion:	all Partners, WP-partners, EC and general public
Status:	Final
DOI:	10.48440/gfz.4.8.2023.009
License information:	CC-BY-4.0
Recommended citation:	Vosper, M., Kummerow, J., Demir, M.M., Tjelta, M., The H2020 REFLECT project: Deliverable 1.4 - Silica dissolution and precipitation. GFZ German Research Centre for Geoscience; DOI: 10.48440/gfz.4.8.2023.009
ORCID:	Morten Tjelta: ORCID: 0000-0002-3376-6702 Julianne Kummerow: Scopus-ID: 36446009700
Related Data:	Tjelta, Morten, & Viig, Sissel Opsahl. (2023). Silica dissolution and precipitation kinetics in hot geothermal conditions (1.0.0) [Data set]. Zenodo. https://doi.org/10.5281/zenodo.8341449 Vosper, M., Bateman, K., & Kilpatrick, A. (2023). Silica dissolution under a flow of pure water at pressure and temperature conditions relevant to geothermal energy extraction [Data set]. Zenodo. https://doi.org/10.5281/zenodo.10212982

Revision history	Author	Delivery date	Summary of changes and comments
Version 01	MV	29.09.2023	Compilation of all chapters and conclusion.
Version 02	MV	29.11.2023	Addition of data publication reference; correction of two references and two figures

Approval status			
	Name	Function	Date
Deliverable responsible	Matthew Vosper	WP Lead, UKRI/BGS	29.09.2023
Reviewer	Mustafa M. Demir	Review of Chapter 2	25.09.2023
Reviewer	Simona Regenspurg	Review of chapter 3	18.09.2023
Reviewer	Matthew Vosper	Review of chapter 4	25.09.2023
Reviewer	Morten Tjelta	Review of chapter 5	20.09.2023
Project Coordinator	Katrin Kieling	Project manager	29.09.2023

Table of contents

LIST OF FIGURES

LIST OF TABLES

1 Executive Summary

This report is a published product of the 'REFLECT' project – a Horizon Europe project which aims to inform the processes of geothermal energy extraction by determining the effect of relevant fluid properties and reactions in order to enhance predictive geochemical modelling and thus the energy exploitation and life-time of geothermal power plants.

One of the most significant technical obstacles encountered in geothermal power generation is scaling of pipelines due to the polymerisation and precipitation of dissolved silica. This report describes dissolution and/or precipitation behaviour of silica in contact with pure water (BGS), saline solution (IFE, GFZ) and metal silicate solutions informed by real geothermal samples from the Tuzla region of Türkiye (IZTECH). Dissolution was studied under both sub- and supercritical conditions (100—495°C, 75—450 bar). With respect to pure water it was found that for any given pressure the temperature at which maximum kinetic dissolution of silica occurs can be predicted straightforwardly from the density of pure water under those conditions. Dissolution rate constants are reported for saline solutions at a range of pressures and temperatures.

The rates of precipitation of silica from metal silicate solutions were studied in the presence of various metal ions. It was found that rate constants may be increased by a factor of up to 10 in the presence of certain species, while sodium has the opposite effect. pH was also found to have a significant effect, with moderately acidic conditions suppressing polymerisation and therefore precipitation.

In addition to traditional photometric methods for monitoring aqueous silica concentration the potential of *in situ* Raman (BGS) and conductometric (GFZ) methods for the monitoring of aqueous silica were assessed. Raman spectroscopy was found to have potential for monitoring silica content and speciation, and conductometry was found to have potential for monitoring processes of complexation and precipitation.

2 Pure Water – Silica Flow Experiments and Assessment of in line, *in situ* Silica Monitoring by Raman Spectroscopy

Matthew Vosper, Keith Bateman, Andrew Kilpatrick
SEM by Alicja Lacinska, BET/N_2 by Simon Kemp and Monty Pearson
UKRI British Geological Survey, UK.

2.1 Introduction

Understanding the behaviour of silica (SiO_2) in contact with water flowing at high temperatures and pressures is necessary for the avoidance of silica scaling in pipes carrying extracted water in geothermal energy systems. It is necessary to know under what conditions the greatest concentrations of silica are likely to be dissolved, and whether depressurisation and cooling of water after extraction is likely to move the solution into a regime that can no longer sustain such concentrations, leading to precipitation. Furthermore, it would be useful if the quantity of silica in extracted water could be monitored continuously *in situ* – at full temperature and pressure in the working pipeline.

This part of the report provides new insight into the behaviour of pure water in contact with silica in a flow system under conditions relevant to geothermal energy extraction, and assesses the potential of Raman spectroscopy as an in-line *in situ* monitoring tool. We have found that the point of greatest dissolution at a given pressure can be predicted very simply from the density of pure water. We also find that a Raman method does indeed have quantitative potential, however further technical hurdles need to be overcome in order to realise that potential for industry.

2.2 Starting Materials and Analytical Methods

2.2.1 Starting Materials

Silica was obtained from Fluka™ in the form of an acid-purified sand fraction with grain sizes from 150 to 400 µm diameter. This quartz sand was further acid washed by boiling in 6% HCl solution and the grains were subsequently sieved to separate a size fraction of 125 to 250 µm diameter. Adhered fines and some black particles were separated by further acid washing, sonication in deionized water and decanting of the resulting top fluid. The quartz was then washed five times with deionized water agitated by a magnetic stirrer, followed by further sonication and decanting. Finally, the quartz was thoroughly dried at 40°C.

The deionized water used was of resistivity 18.2 MΩ generated using an Avidity™ Laboratory Water System. The silica standard had a concentration of 1005 ± 5 g/mL and was supplied by Santa Cruz Biotechnology®.

2.2.2 Analytical Methods

Measurements of silica concentration in flow experiments were made using photometry of the yellow β-silicomolybdic acid complex formed by the reaction of sodium molybdate with silica in the presence of sulfamic acid when the pH is close to, but above, 1 (Figure 2.1):

$$SiO_2 + 12NaMoO_4 + 24SO_2NH_2OH \rightleftharpoons H_8SiMo_{12}O_{40} + 24SO_2NH_2ONa + 10H_2O$$

A Macherey-Nagel PF-12 Plus photometer was used, set to programme 5342, which measures SiO_2 concentration in the range 10—200 mg/L and which is calibrated for the reagents used (obtained from Macherey-Nagel as a recommended set for this program). To measure concentrations greater than 200 mg/L, samples were diluted with deionised water as required (two- or four-fold) and the instrument data corrected (multiplied up) accordingly.

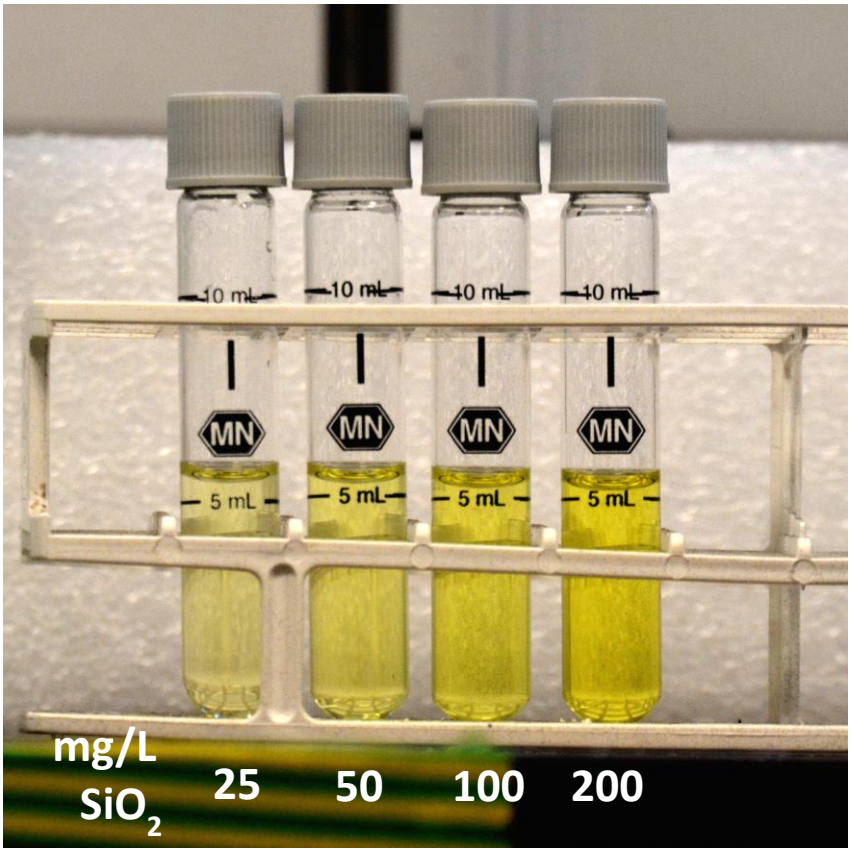

Figure 2.1. β-silicomolybdic acid formed from different silica concentrations.

Scanning Electron Microscopy (SEM) analyses were performed at the Petrography Laboratories of the British Geological Survey, using Zeiss Sigma 300 VP-FEG with a dual Bruker Quantax XFlash 6|30 Energy Dispersive Spectrometer (EDS) system. Samples of pre- and post-test materials were analysed in the form of carbon sputter coated (≈25 nm thick) grain mounts. The SEM was operated under conditions of high vacuum (1.2×10^{-6} Torr) at accelerating voltage ranging from 5-15 kV, with 7 - 10 mm optimal analytical working distance, depending on the mode of imaging, and an X-ray detector take-off angle of 35°. High resolution imagery was performed using an in-lens secondary electron detector. Qualitative chemical analyses of the mineral phases were performed using SDD EDS Bruker system, Esprit version 2.1.

Raman experiments were conducted using an excitation wavelength of 532 nm (green), generated by an Ocean Optics diode laser (model LASER-532-IP-LAB) with a stated power output of >50 mW and spectral linewidth of <0.5 nm. Initial experiments using cuvettes were conducted with a standard (RIP-RPB-532-FC) InPhotonics Raman probe with a focal length of

7.5 mm. Experiments using the high temperature apparatus were conducted using an InPhotonics high temperature Raman probe fitted with an InPhotonics high temperature telescopic extension rated to 204°C, and giving a working distance of 100 mm. Raman scattering was measured using an Ocean Optics QEPro High Performance Spectrometer with a 50 µm slit giving 23 cm^{-1} resolution, operated using Spectragryph© software.

The surface area of the samples was determined using the amount of nitrogen adsorbed onto a solid surface at monolayer coverage from a multipoint plot of adsorption isotherm data using the BET/N_2 method, named after its inventors Brunauer, Emmett and Teller (Brunauer et al., 1938). Approximately 2 g subsamples were degassed overnight in a vacuum oven at 60°C and then further degassed using a Micromeritics Gemini VacPrep for a least 1 hour at 60°C prior to analysis. Surface area analyses were conducted using a Micromeritics Gemini VI 2385C system. The samples were run on a 10-point adsorption pressure point program with a 10-second equilibration time.

2.3 Experimental

2.3.1 Flow Experiments

2.3.1.1 Background

The kinetics of silica dissolution in natural bodies of silica will depend on the particular chemical and morphological properties of the silica at that particular site: These include the exposed surface area of the silica, its crystal structures, heterogeneities and impurities, the surface morphology and the concentration of high energy/reactive sites per unit surface area. For these reasons the absolute values of silica concentration in extracted waters may not be consistent between different sites under the same conditions (unless the water is saturated). Nevertheless, it is possible to assess trends and identify the conditions under which the highest silica concentrations are likely to occur.

Data already exist for the saturation of silica in water, and Fournier and Potter (1982) produced an equation to model this. However, this model has a *pT* (pressure-temperature) range far greater than that which is of interest to geothermal energy extraction, and its accuracy is uncertain in that much more restricted region. Since the region of interest for geothermal energy extraction includes the critical point of water (374°C, 221 bar), around which properties are much harder to model, additional data on the system is much needed.

The data presented covers the region from 200—450°C and 150—450 bar. The combination of flow rate and the amount of material used produced concentrations that are kinetically controlled (i.e. below the saturation level).

2.3.1.2 Experimental Approach

Silica was dissolved using the flow system depicted in Figure 2.2. The prepared silica grains were packed into a column constructed from a 105 mm section of 3/8” Hastelloy® tube, fitted at each end with a 1 mm thick, 3/8” Hastelloy® frit with 2 µm grating to prevent the migration of undissolved sample from the column. Other tubes and fittings were of 1/8” 316 stainless

steel, with the valves and associated fittings supplied by HiP High Pressure Equipment, and all tubes and other fittings supplied by Swagelok®.

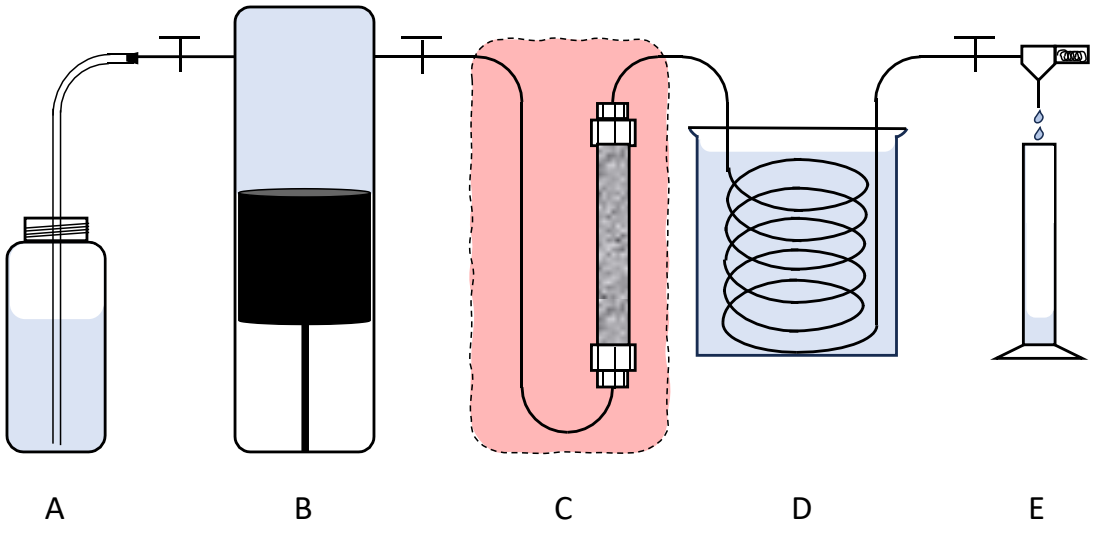

Figure 2.2. Schematic diagram of silica dissolution rig.
A: Deionised water (18.2 MΩ) to feed pump. B: Teledyne ISCO® syringe pump. C: Heated section of the rig including silica filled column. D: Quenching beaker. E: Spring-loaded pressure relief valve dripping into measuring cylinder.

The pump was a Model 260D Teledyne ISCO® syringe pump with a volume of 250 mL and a maximum pressure of 500 bar. The pump was filled with 18.2 MΩ deionized water and set to run at a constant flow rate of 1 mL/min. The pressure was regulated by an externally-adjustable spring-loaded pressure relief valve (Swagelok®) at the terminal point of the rig which dripped the resulting silica solution into a measuring cylinder.

The temperature was controlled by a length of BriskHeat® heating tape powered by a 10 A Electrothermal® power regulator wrapped around the silica-filled column, and 25 cm of tubing before and 5 cm tubing after the column. The heated section of the rig was wrapped tightly in a thick blanket of quartz wool insulation.

Between the heated section of the rig and the pressure regulator the tubing was passed in a coil through cold water to quench the temperature.

The resulting solution was allowed to drip through the outlet of a spring-loaded pressure relief valve that also served to control the pressure in the system. Once the desired conditions for each experiment had been attained, three times the system volume of water was allowed to flow before sample collection started. Once 10 mL of sample had been collected the solution was analysed by photometry as described in Section 2.2.2.

2.3.2 Construction of an *in situ* Raman Reaction Vessel

To assess the potential of an in-line *in situ* silica monitoring process using Raman spectroscopy, we designed and constructed a vessel in which silica could be dissolved and the dissolution process could be monitored continuously.

The vessel is a vertically-oriented cylindrical chamber with a closure at each end, face sealed with a metal C-ring (Figure 2.3). The closures are held in place by a steel collar secured by a circular array of cap head screws. A sapphire window (Figure 2.4) attached to the top enclosure allows a Raman laser to probe the vessel contents and Raman scattered light to return to the probe. The top closure also included two access ports. The bottom closure contained a port for draining fluid and another port to which an internal bellows was welded (Figure 2.5).

Quartz grains are added to the cell beneath the bellows, and the cell filled with fluid at temperature and pressure and allowed to equilibrate. Raman spectra are obtained through the top window and samples withdrawn to allow measurement of silica concentration by photometry to verify the Raman measurements. The bellows is filled with fluid and held at a fixed pressure so that it will expand to keep experimental pressure constant during sampling. The internal volume of the vessel is therefore variable between 125 and 200 mL. The electric trace heating array was commissioned from Cross Electrical, Keyworth, UK.

To assess the method under conditions relevant to geothermal energy extraction, the cell was designed to withstand pressures up to 500 bar at temperatures up to 500°C. For this reason, all parts of the cell intended to be in contact with the fluid were machined from Hastelloy C276. The closure rings were machined from high carbon steel (EN24T), which has very high tensile strength but is dissimilar from Hastelloy C276 to prevent galling of the threaded joint.

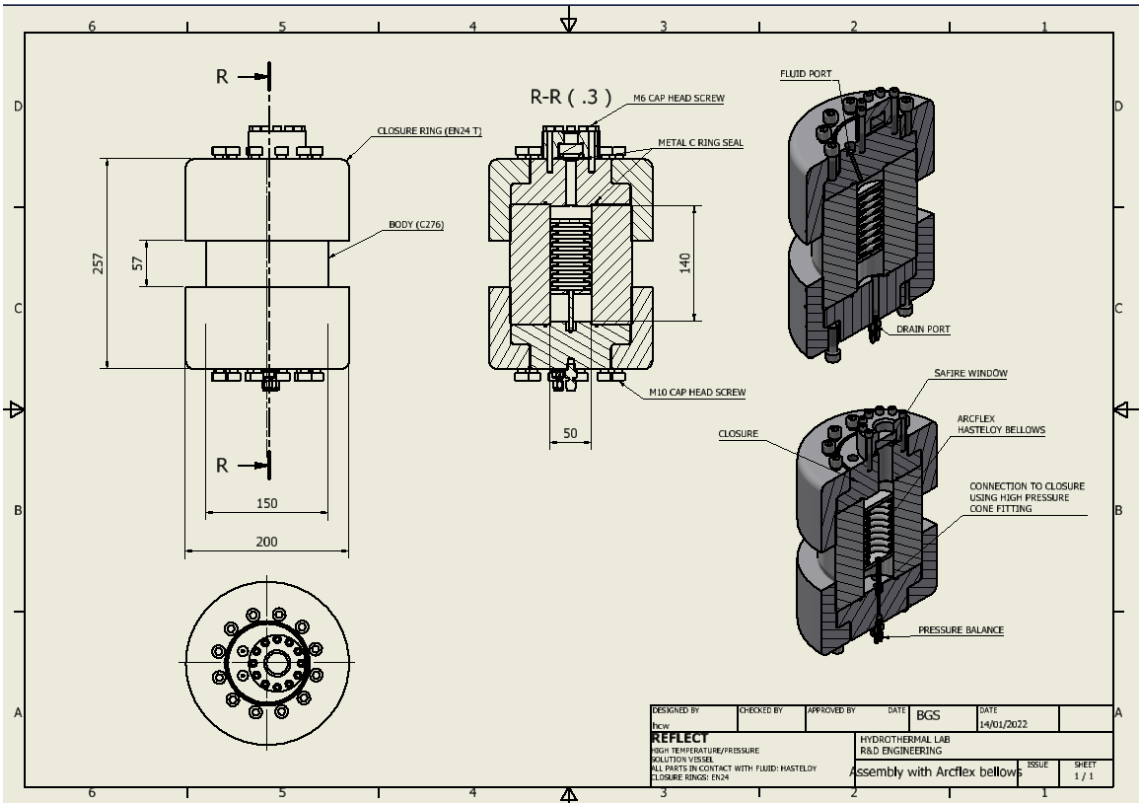

Figure 2.3. Sectional assembly of the Raman vessel.

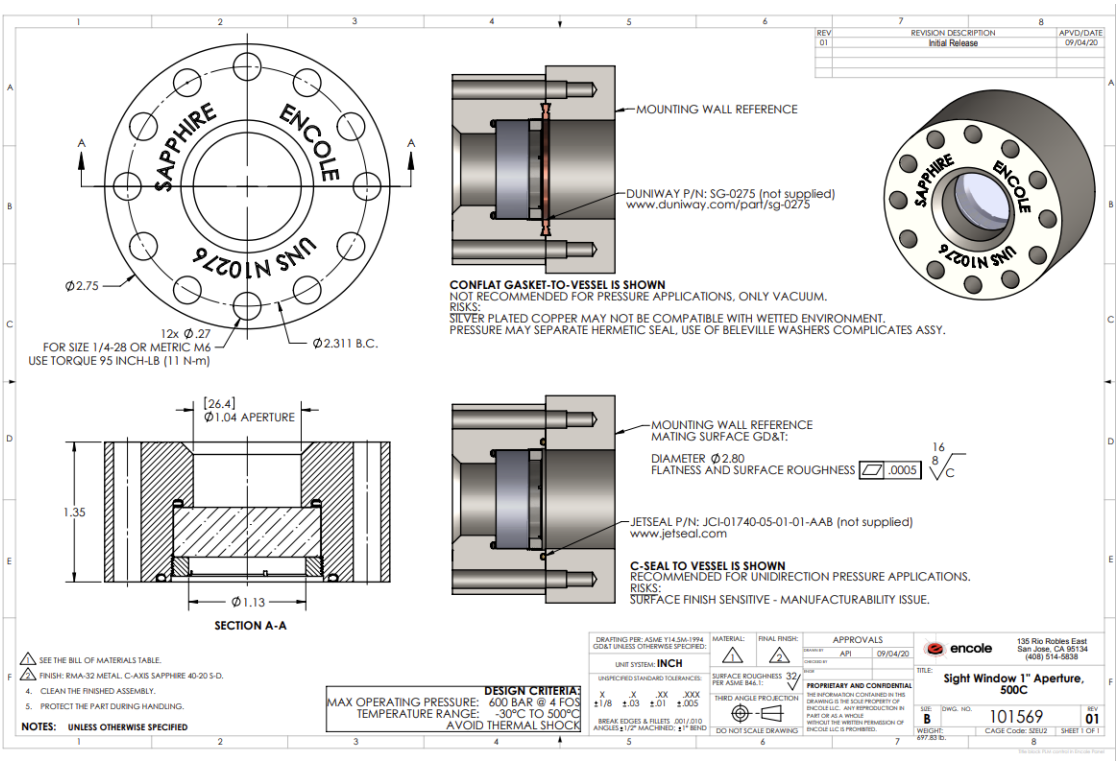

Figure 2.4. Detail of sapphire window; supplied by Encole, San Jose CA 95134

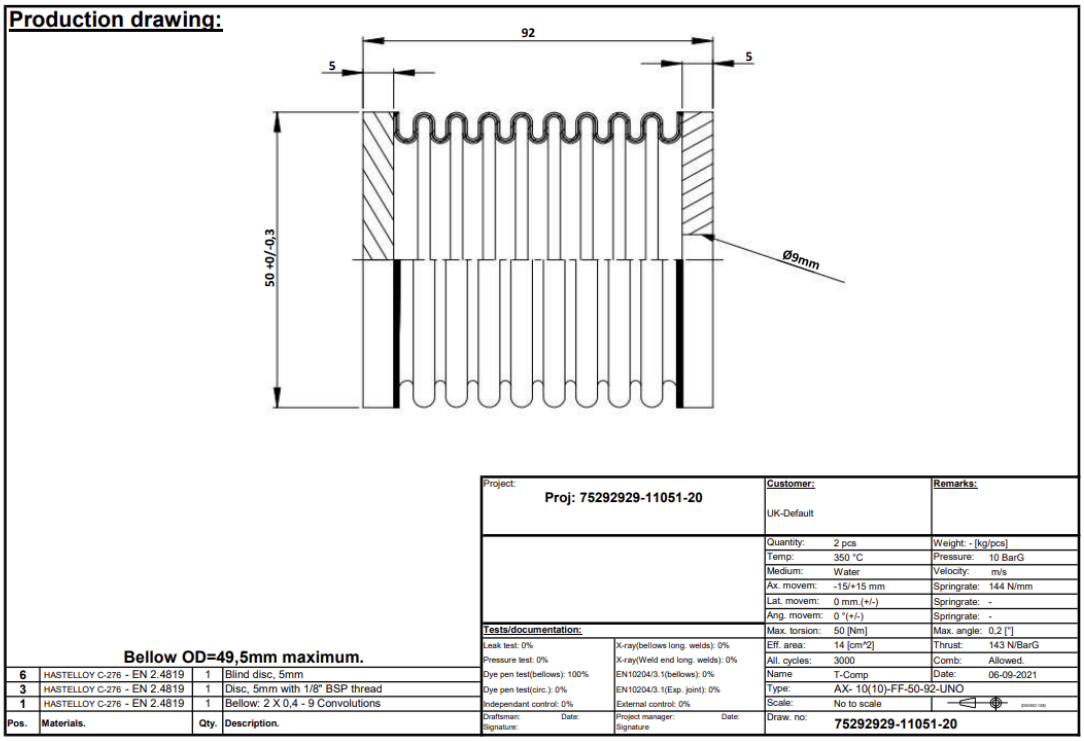

Figure 2.5. Bellows; supplied by Arcflex 3 Tower Road, Meaford Business Park, Stone, Staffordshire, ST15 0WQ

2.4 Results and Discussion

2.4.1 Flow Experiments

2.4.1.1 Observed variation of silica concentration with pressure and temperature

Experiments were performed in the range 150—450 bar and 200—450°C. The quantity of silica initially charged to the column was 6.76 g, and the flow rate was set to 1 mL/min.

Isobars of the silica concentration are plotted against temperature in Figure 2.6, and the density of pure water at the measured *pT* combination in Figure 2.7 (calculated using the IAPWS-95 formulation of Wagner and Prüß (2002)). Data at 370°C and 374°C on the 200 bar isobar are omitted from Figure 2.7 because it is thought likely that they represent two-phase flow. Furthermore, the silica concentration recorded at 148 bar and 344°C is plotted against the density of pure liquid phase water at 150 bar and 342°C (the closest integer point on the phase boundary to the measured condition): this is because the solubility measurement clearly indicates a liquid phase measurement although pure water would narrowly be in the vapour phase. This discrepancy could be explained by a small shift in the phase envelope due to the dissolution of silica, in addition to any uncertainties in the *pT* measurement.

Figure 2.6 shows that, although our solutions were not saturated, the system follows the typical pattern for solubility isobars of a minor component in a fluid. Below the critical

pressure (221 bar) the concentration of silica in solution in the liquid phase increases with temperature until the phase transition temperature is reached; above that temperature, in the vapour phase, the silica concentration is greatly and discontinuously lower but also increases with temperature. Just above the critical pressure the silica concentration increases to a peak near the critical temperature (374°C) and then falls precipitously (but continuously) before rising again. As the pressure increases further beyond the critical pressure the peak broadens and shifts towards higher temperatures. The silica concentration was even observed to fall at temperatures around 350-370°C when the pressure was increased from 350 to 450 bar as the peak shifted to the right, although this effect may be exaggerated by changes to the bulk material during the run, as discussed in Section 2.4.1.2.

The plot of this data against the density of pure water is of particular interest (Figure 2.7). Rather than the solubility peak migrating across the plot, all isobars are aligned showing a peak when the density is between 0.5 and 0.6 g/mL. This provides a useful 'rule-of-thumb' for locating the highest concentrations of silica that will be obtained in this particular range at a given pressure. Figure 2.8 shows the region of *pT* space at which water has a density in this range. Moving isobarically away from the area bounded by the red lines involves moving to a region that generates lower silica concentrations. This does not necessarily mean that precipitation will occur in a real system because water may not be saturated with silica to start with, however it shows the direction of temperature change that poses the greatest risk of silica precipitation. In general, the measured concentration of dissolved silica increases with pressure, but further research is needed to determine, for example, how far pressure needs to increase to outweigh the effect of temperature moving away from the red bounded region under any particular set of conditions. Further research would also be required to determine whether there is an effect of flow rate on the exact position of the peaks with respect to density observed in Figure 2.7.

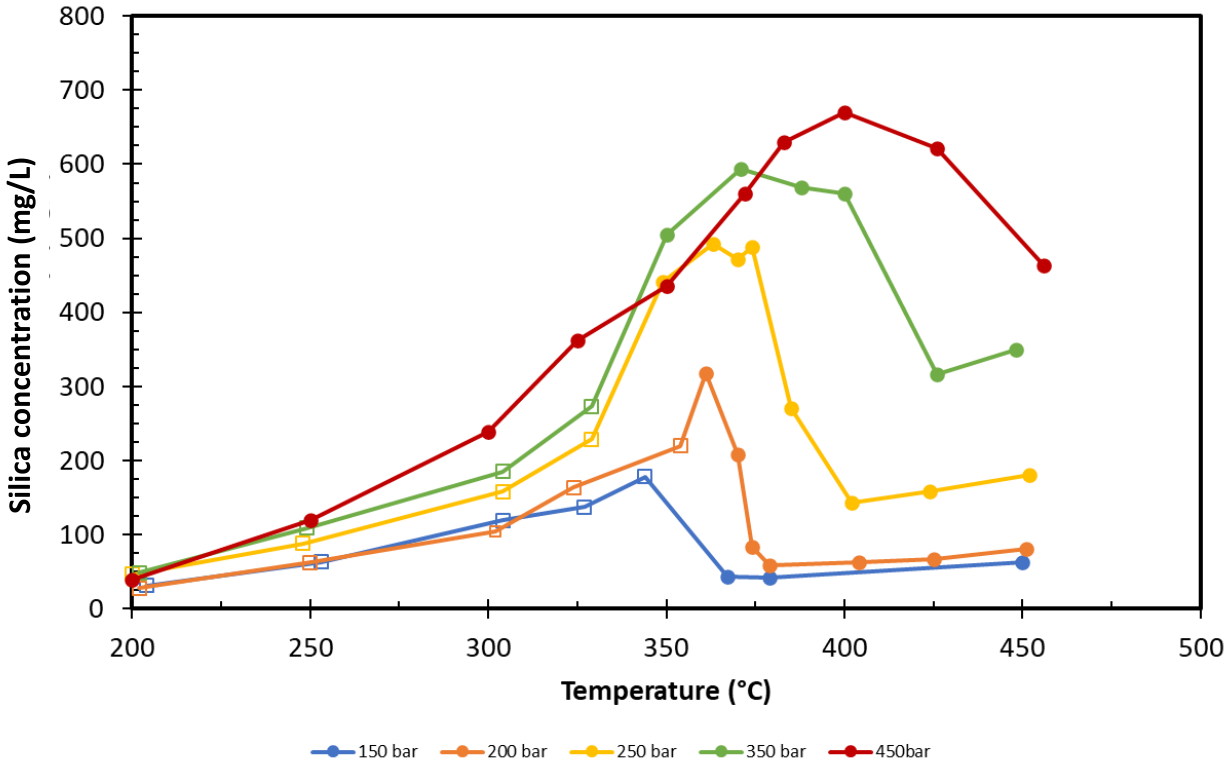

Figure 2.6. Dissolved silica concentration isobars plotted against temperature.

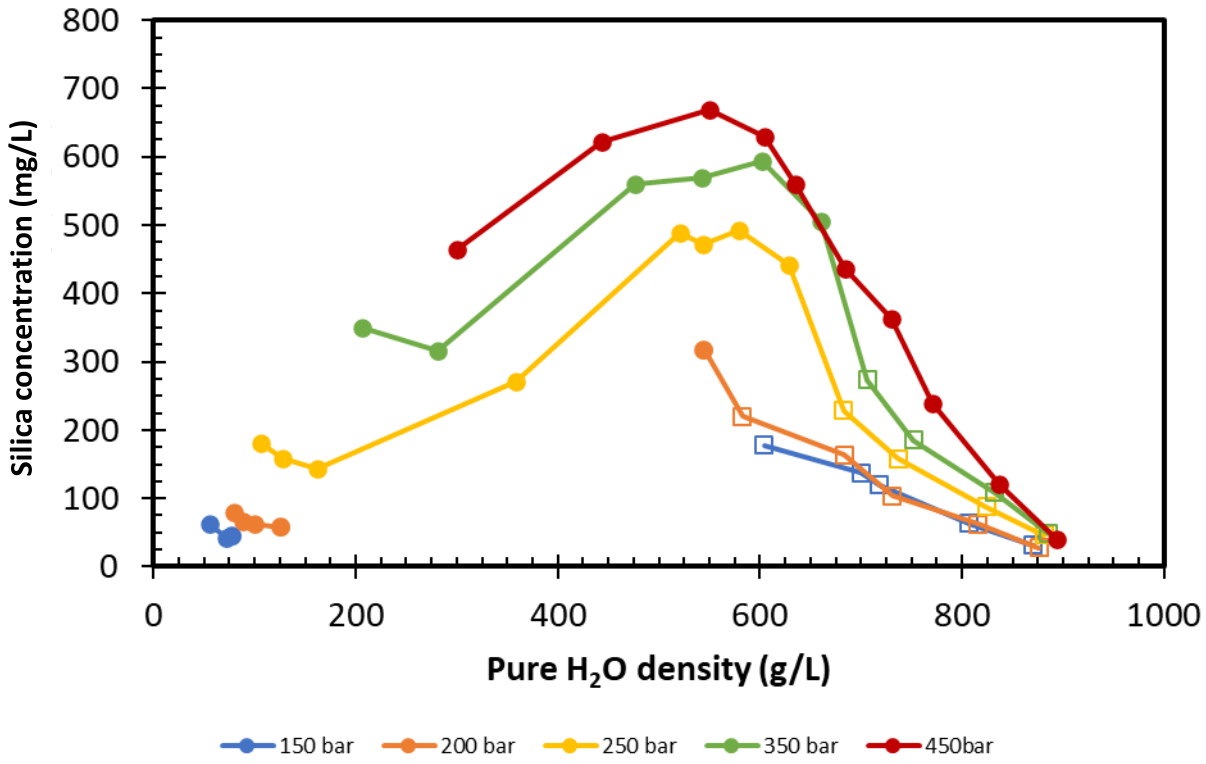

Figure 2.7. Dissolved silica concentration plotted against the density of pure water.

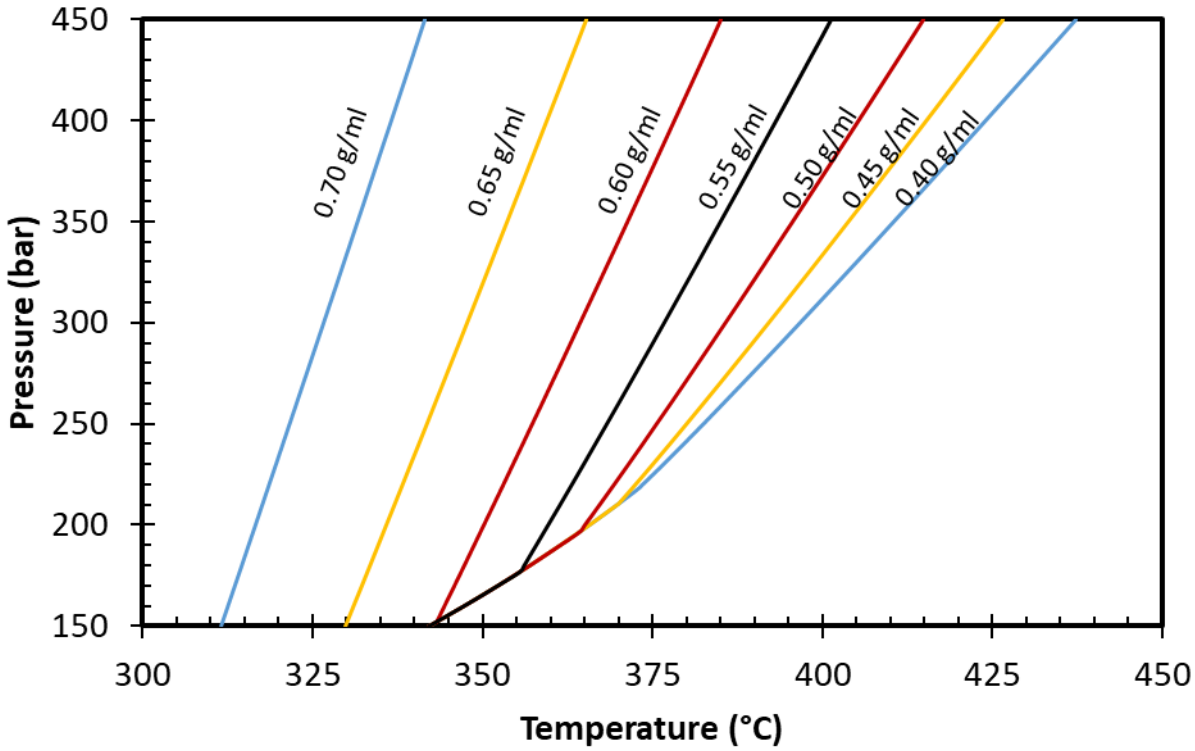

Figure 2.8. Isochores of pure water according to the IAPWS-95 formulation of Wagner and Prüß (2002) calculated using REFPROP software (Lemmon *et al.,* 2018). Silica dissolution decreases when moving isobarically away from the region bounded by the red isochores.

2.4.1.2 Effect on bulk material

At the end of these experiments, the expected quantity of silica lost through dissolution during the run was estimated using the measured solubilities coupled with the duration for which the apparatus had been run at each set of conditions. The mass loss was estimated to be 1.65 g, or 24.4%. The remaining silica was then retrieved from the column and thoroughly dried before weighing. It was found that the actual mass lost through dissolution agreed very well with the calculated estimate, being 1.73 g, or 25.6%. The mass present at any point in the run can therefore be estimated with reasonable accuracy.

Since the solutions produced in these experiments were not saturated with silica, this decrease in solids should have reduced the overall surface area of silica enough to appreciably reduce the measured silica concentrations in experiments performed later. Therefore the order in which measurements were made must be considered when interpreting the measurements. This effect is clear in Figure 2.6 and 2.7 In general, the higher temperatures of each isobar were measured first, from the lowest pressure to the highest, and then the lower temperatures of the same isobars from the highest pressures to the lowest. The merit of this approach is that it provides a test for changes in the bulk material, which may be detected if the isobars fail to 'join up' in the middle.

Data measured after the completion of the 450 bar isobar are shown as open squares in Figure 2.6 and 2.7. It appeared clear that these values were significantly lower than might be

expected when compared with the higher temperature points. Therefore, at the end of the run, further points were measured that were directly comparable to points taken early in the experiment: these typically displayed a reduction of 30—35% in the dissolved silica concentration.

Such a reduction in measured concentration cannot be explained simply by a reduction in surface area. The specific surface area (BET/N_2) of the quartz increased slightly over the course of the run from 0.0781 ± 0.0041 to 0.0881 ± 0.0029 m^2/g, so that the *total* surface area only decreased by 17%. This suggests that the density of reactive sites per unit surface area may also have approximately halved.

Scanning electron microscopy analysis demonstrates that several different dissolution mechanisms were in operation during the experiments. SEM images in Figure 2.9 are arranged by columns A-C and rows 1-3. Images of the starting material (A1, B1) show clean surfaces and sharp edges. There are also fractures with a conchoidal, stepped shape. Images of material retrieved after the experiments (C1 and rows 2 and 3) show dissolution features that fit into two separate categories. Those shown in row 2 appear to reflect features of the initial quartz material including concentric conchoidal pits that resemble the conchoidal fractures of the starting material, and a straight slot (C2) that probably also reflects an initial cleavage. Those shown in row 3 at higher magnification show dissolution features with triangular (C2, A3) or rectangular (B3, C3) surface openings, and similar shallow etchings. It may be that high energy sites within original fracture points became exhausted during the high dissolution experiments, leaving only the slower etching/pitting mechanisms to operate during the later experiments.

These observations show how some thermophysical conditions of geothermal energy extraction may alter important properties of the affected silica over time. They also demonstrate the importance of considering relative trends over absolute values in these research areas.

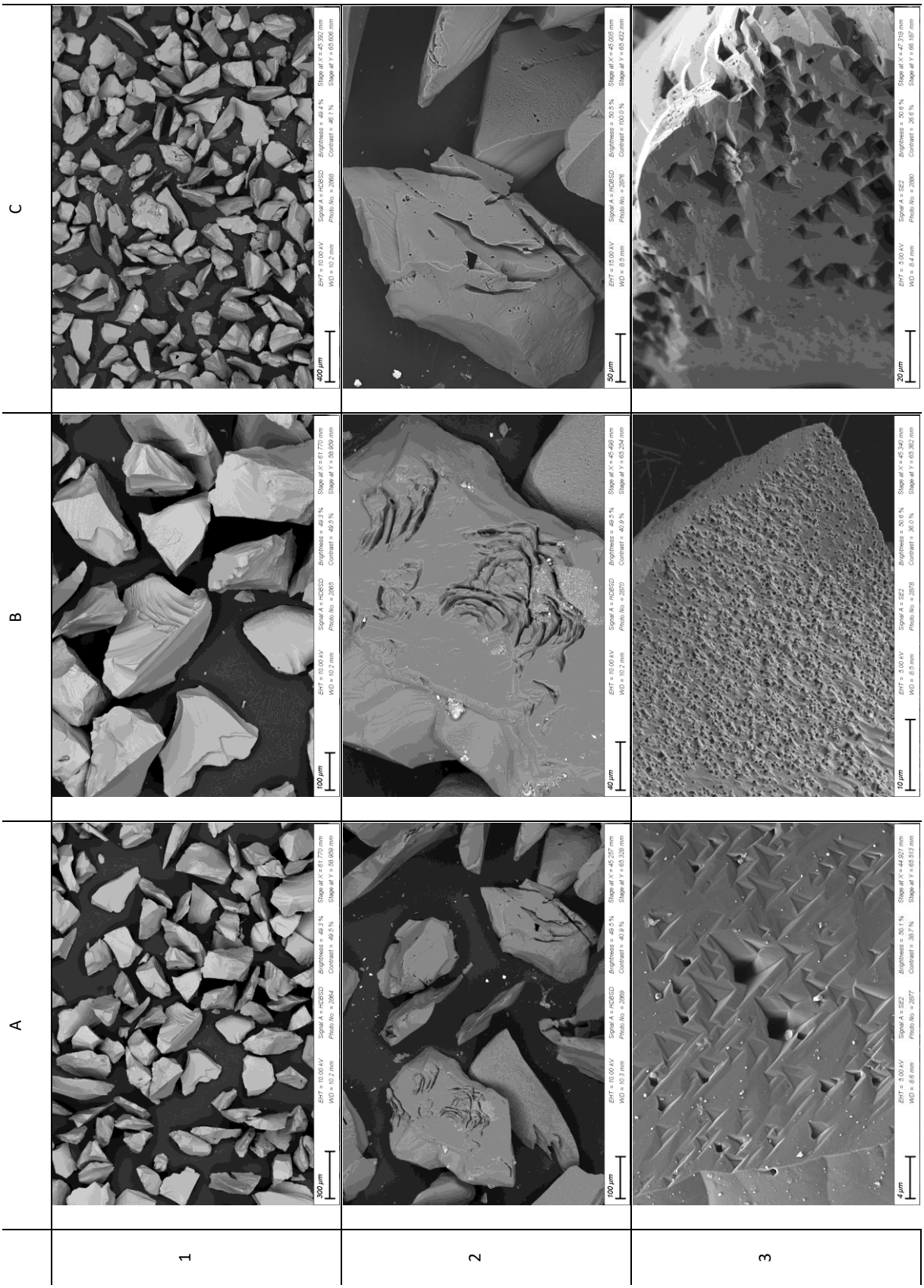

Figure 2.9. SEM images of quartz material before (A1, B1) and after (all other images) flow experiments. See text for details.

2.4.2 Raman Experiments

2.4.2.1 Detection of silica Raman bands in cuvettes

Zotov and Keppler (2000), Hunt *et al* (2011) and recently Takahashi *et al.* (2022) have deployed Raman spectroscopy to detect silica at high pressure and temperature in diamond anvil cells. The detection of dissolved silica in a diamond anvil cell presents a different technical challenge to the detection of silica in a pipeline. An *in situ* method would involve directing a Raman laser through a sapphire window in a pipeline wall into a large volume of flowing fluid. A diamond anvil cell is a small piece of apparatus containing a very small quantity of sample (typically just a few cubic microns). To detect dissolved silica, these researchers deployed a confocal Raman system to intensify the beam onto the smallest possible spot, they also deployed high powered lasers (400mW output for Hunt *et al*) at short non-standard wavelengths (514.5 nm for Zotov and Keppler, 488 nm for Hunt *et al*).

Confocal Raman systems are disadvantageous in terms of bulk, complexity and cost compared to standard Raman systems. In a geothermal plant pipeline, the quantities of fluid involved are much larger, and it is therefore reasonable to consider whether a simple Raman probe with a more typical laser might be sufficient. The wavelength used here, at 532 nm, is the shortest wavelength conventionally deployed for Raman spectroscopy, offering a stronger Raman signal than 785 or 1064 nm: we did not experience any problems with fluorescence during our experiments.

Initial tests to detect the silica peak were performed in plastic cuvettes using a 1000 mg/L silicon standard at room temperature and pressure, and the same standard diluted by half. The cuvette was held in a 2D-adjustable holder, with the focal point of the laser positioned in the centre of the cuvette to reduce signal from the cuvette walls and maximise signal from the sample. The peak was detected at a Raman shift of 785 cm^{-1} using an average of six 10-minute exposures. This peak in Figure 10 is the tetrahedral Si—OH stretching mode of the $Si(OH)_4$ monomer (Takahashi *et al.*, 2022). The other peaks visible in Figure 2.10 are due to the plastic of the cuvette.

The peaks of the 1000 mg/L silicon standard, undiluted and diluted to 500 mg/L, are shown in Figure 2.10 after baseline correction and subtraction of peaks due to pure water and the cuvette walls. These peaks are small and subject to noise, however with a baseline set from 750—820 cm^{-1} the height of the 500 mg/L peak is approximately 55% of the height of the 1000 mg/L peak, suggesting a probable linear relationship between concentration and peak height.

The signal to noise ratio was improved by using a quartz glass cuvette (the spectrum of this cuvette is far simpler than the plastic, and the peak due to the solid silica of the quartz cuvette is easily distinguishable from the dissolved silica, being found at 926 cm^{-1}). A further improvement was made by using three 30-minute exposures rather than six 10-minute exposures. In this spectrum (Figure 2.11) it is also possible to see additional peaks between 1000 and 1100 cm^{-1}. By comparison with the work of Hunt *et al* (2011) these are identified as evidence of deprotonated monomer species, most likely $Si(OH)_3O^-$.

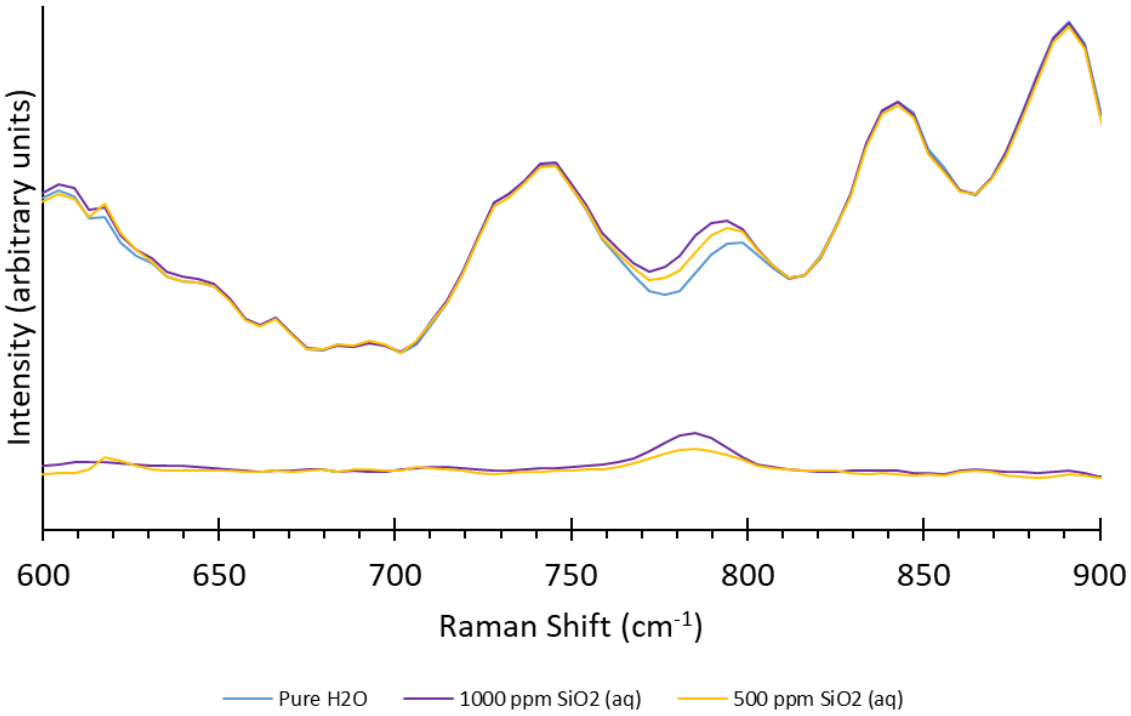

Figure 2.10. Raman spectra of pure water and 1000 and 500 mg/L aqueous silica in a plastic cuvette (upper), and the silica peaks at 785 cm^{-1} after subtraction of the pure water spectrum (lower).

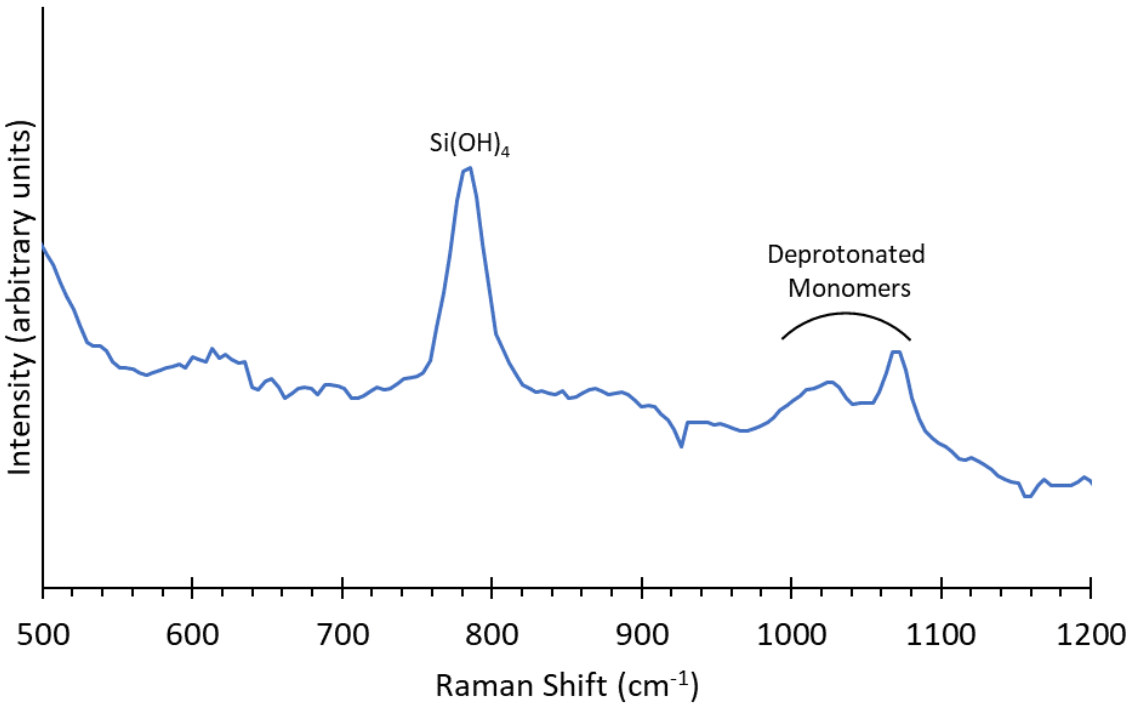

Figure 2.11. Raman spectrum of 1000 mg/L aqueous silica showing peaks suggestive of deprotonated monomers

2.4.2.2 Attempted measurements using high pressure and temperature equipment

The construction of the high pressure, high temperature Raman cell was subject to lengthy delays due to manufacturer challenges and ongoing impacts of the COVID-19 pandemic. When the cell was completed and delivered there was little time left to create a fitted heating jacket and obtain pressure certification for the cell. Nonetheless, initial attempts have been made to detect the silica Raman band in 1000 mg/L silica standard at room temperature and pressure using the high temperature probe and telescopic extension described in Section 2.3.2.

These initial experiments have not yet been successful in detecting the silica band. It was noted that the signal from the water was considerably weaker than it had been using the cuvettes. This was judged using the bending peak at 1635 cm^{-1} (the OH stretching peaks were saturated by the long exposures, as they had been in the cuvette experiments). The silica peak, which is much smaller than the water bending peak, was therefore undetectable amid the noise.

This is most straightforwardly explained by considering the working distances of the probes in the two set ups. In the cuvettes, the probe was positioned just 2.5 mm from the cuvette, the beam was contained in the very small chamber of the cuvette holder, and was focussed on the sample at a point just 7.5 mm from the probe providing relatively little opportunity for photons to 'escape'. In the high temperature set up the probe is distanced from the sample using a telescopic extension to prevent damage due to exposure to high temperatures. As a result the working distance is a fixed 100mm Since there is a much greater distance between probe and sample there is likely to be a much greater proportion of the Raman scattered light that fails to return to the probe, greatly reducing the total signal.

The Raman spectrum of the sapphire windows near 785 cm^{-1} is more complex than that of the quartz cuvette, but simpler than that of the plastic cuvette. The spectrum of the sapphire windows is not expected to pose a problem for the disambiguation of this band if the signal strength can be improved through future research.

2.5 Conclusions

By analysing the pure water-silica system in a flow regime below saturation we have identified that, for any given pressure in the range of this study, the greatest concentration of silica is generated when the density of pure water is approximately in the range 0.5—0.6 g/mL. Although it is not known whether the location of this maximum is affected at all by flow rate, this observation suggests that in a kinetically controlled regime it is possible to provide a very useful 'rule of thumb' allowing the region of maximum dissolution to be predicted simply from the thermodynamic conditions at any particular pressure. It also allows a simple prediction of whether increasing or decreasing the temperature isobarically at any point in the region is likely to lead to an increase or a decrease in silica concentrations. The greatest rate of increase of concentration with pressure occurs when both the pressure and temperature are near to the critical point. Our experiments demonstrate that the process of geothermal energy

extraction is itself capable of altering the properties of silica in ways that can change the rate of its dissolution over time.

It has also been found that a relatively simple Raman spectroscopic set-up is capable of detecting silica in pure water. Bands associated with deprotonated monomer species have also been detected, suggesting that Raman spectroscopy has the potential to monitor several silica species in solution. However, our study required very long exposures to measure these peaks (six exposures of 10 minutes or three exposures of 30 minutes). For an industrial scale in-line monitoring system this will need to be improved. These long exposures were necessitated by the weakness of the Si—OH stretching mode at 785 cm^{-1}. This issue is compounded by our initial experience with the high pressure and temperature apparatus, with which we were unable to detect the silica band due to a reduced overall signal, even with these high exposure times.

The potential of the method has been demonstrated, but technical hurdles remain to be overcome to make the method practical for in-line *in situ* monitoring of extracted geothermal water. It is clear that operation of a Raman method at high pressure and temperature requires a means of ensuring maximum return of Raman scattered light to the probe. This could take the form of a fitted light guide and alternative methods of insulating the probe from heat that would allow it to be placed closer to the window. The long exposure times can also be shortened if the signal-to-noise ratio is reduced in alternative ways, such as by using a higher powered or shorter wavelength laser.

The equipment and experience developed over the course of this project could be used to investigate further the kinetic and thermodynamic behaviour of the silica-water system, including the effect of flow rate, and to study with greater precision the area around the critical point. Further demonstration of the Raman method could involve the detection of silica in real or simulated geothermal water to assess the impact of other common solutes.

2.6 References

Brunauer, S., Emmet, P.H. & Teller, E. (1938). Adsorption of Gases in Multimolecular Layers. *Journal of the American Chemical Society*, 60.

Fournier, R.O., & Potter II, R.W., (1982) An equation correlating the solubility of quartz in water from 25°C to 900°C at pressures up to 10,000 bars. *Geochimica et Cosmochimica Acta*, *46*(10). https://doi.org/10.1016/0016-7037(82)90135-1

Hunt, J.D., Kavner, A., Schauble, E.A., Snyder, D., & Manning C.E., (2011) Polymerisation of aqueous silica in H_2O-K_2O solutions at 25-200°C and 1 bar to 20 kbar. *Chemical Geology 283*. https://doi.org/10.1016/j.chemgeo.2010.12.022

Lemmon, E.W., Bell, I.H., Huber, M.L., McLinden, M.O. NIST Standard Reference Database 23: Reference Fluid Thermodynamic and Transport Properties-REFPROP, Version 10.0, National Institute of Standards and Technology, Standard Reference Data Program, Gaithersburg, 2018.

Takahashi, N., Tsujimori, T., Kamada, S., Nakamura, M., (2022) In-situ Raman spectroscopic analysis of dissolved silica structures in Na2CO3 and NaOH solutions at high pressure

and temperature. *Contributions to Mineralogy and Petrology, 177,* https://doi.org/10.1007/s00410-022-01892-y

Wagner, W., & Pruß, A., (2002) The IAPWS Formulation 1995 for the Thermodynamic Properties of Ordinary Water Substance for General and Scientific Use. *Journal of Physical and Chemical Reference Data, 31*, https://doi.org/10.1063/1.1461829

Zotov, N., & Keppler, H., (2000) In-situ Raman spectra of dissolved silica species in aqueous fluids to 900°C and 14 kbar. *American Mineralogist 85*. https://doi.org/10.2138/am-2000-0423

3 Rates and Magnitudes of Metal Silicate Precipitation

Morten Tjelta, Sissel Opsahl Viig,
Institute for Energy Technology, Norway

3.1 Introduction

Silica dissolution and precipitation can be mathematically described by kinetic rate laws. In principle, such expressions may be functions of pressure, temperature, pH, salinity and concentrations of reactants and also foreign ions. This report presents the experimental approach taken to obtain silica dissolution rates at different temperature, pressure and salinity.

Quartz dissolution experiments have been carried out in a packed column setup using different flow rates to obtain kinetic information. Conditions ranged from 300 to 400°C with pressures from 75 to 90 bar, covering both gaseous, liquid and supercritical water. The effect of salinity was studied by varying the NaCl concentration from 1 to 30 g/L (referred to ambient water). Rate constants were then converted to precipitation rate constants using theory described in open literature.

Dissolution rate constants were in the range 10^{-9} to 10^{-7} mol/m^{2}s for liquid and supercritical water and 10^{-11} to 10^{-12} mol/m^{2}s for vapor-like water. Calculated precipitation rate constants were two orders of magnitude larger for liquid and supercritical and 3-4 orders of magnitude larger for gaseous water. The qualitative trends are similar for both precipitation and dissolution rates: There is a significant increase from 300 to 350°C, while from 350 to 400°C the temperature effect is small. Above 350°C the effect of cations (NaCl) is small.

3.2 Theory

During geothermal fluid production, changes in temperature and pressure may cause precipitation of solids and thereby influence the flow assurance in the system. In order to predict and mitigate such scaling, reliable models based on sufficient experimental data are highly sought for. In this task, experiments have been carried out to obtain information about silica scaling kinetics in the temperature range 300—400°C with NaCl levels ranging from 1 to 30 g/L.

Due to the complexity of direct precipitation measurements at high temperature, this work describes results of dissolution kinetics experiments which are then related to precipitation using absolute rate theory as described in Ref. [1] and [2]. The ideal experiment would be direct measurement of precipitation kinetics. This should be done whenever possible. At lower temperatures, say up to 200°C, kinetics is fairly slow and it is possible to follow precipitation by analyzing samples. This approach was followed by Ref. [3] when they analysed fluid samples taken as a function of time and measured monomeric silica concentration using the molybdenum blue method. A real fluid of around 250°C with around 600 mg/L SiO_2 was used as a source, but the kinetic measurements were carried out after cooling to a temperature in the range 25—90°C.

At higher temperatures precipitation is expected to occur almost instantaneously when the solution is supersaturated, meaning that any sample taken in practice will be that of the saturated solution. In order to capture precipitation kinetics some *in situ* information, such as a window or a probe, is required. Some labs have developed HPHT reactors with sapphire windows (double or even triple) which could in principle be coupled with an *in situ* method such as Raman spectroscopy. Such a setup has been developed within the REFLECT project and is described in Section 2.3.2.

It can be argued that some solid surface/nuclei (not necessarily silica) are always present in a geothermal stream. Models can therefore be simplified by accounting for only the growth part, i.e. nucleation is not included. Another approach is to include the effect of nucleation as an induction time for precipitation in the models. In theory, nucleation dominates at high supersaturation while growth dominates at lower supersaturation. In practice this probably means that growth is dominating in most parts of the production well where you have gradual changes, while nucleation becomes important where you have sudden changes (high supersaturation), for example after a valve or restriction. Since silica particles are always present in the experiments carried out in this work, the results will be relevant for particle growth.

3.2.1 Relating Dissolution to Precipitation

The theory arguing how results from dissolution experiments can be applied to obtain precipitation information is described Ref. [1] and [2]. Ref. [1] measured silica dissolution up to 300°C in pure water. Kinetic information was obtained by taking fluid samples at intervals to determine the H_4SiO_4 concentration. Based on absolute rate theory, where reactions pass through an activated complex with an energy maximum, a relation between the forward and backward (i.e. dissolution and precipitation) reactions was put forward. The authors noted that their work is valid for silica and relatively pure water, and that the rate constants may be complex functions of pH and salinity. A high value for the Arrhenius activation energy suggests that the reaction rate for precipitation of silicic acid is determined by the Si-O bond strength. The authors therefore concluded that the activation complex must be the same for the SiO_2 forms quartz, cristobalite and amorphous silica and that the precipitation (k_-) is the same for all types, but the SiO_2 dissolution rate constant depends on the type of silica. Precipitation and dissolution (k_+) rate constants are related through the thermodynamic equilibrium constant (K) as $k_+ = K \cdot k_-$.

Ref. [2] also based their precipitation kinetics on dissolution data and a correlation between dissolution, precipitation kinetics and the equilibrium constant. Measurements were carried out at different temperatures using 5 different setups (some for lower and some for higher temperature) up to 255°C. These data were compared with literature data up to 625°C to provide a regression of a quite comprehensive dataset. It was noted that the rate constants have effects of pH, pressure, ionic strength etc. embedded, but that such effects could be deconvoluted with more experimental data available.

3.2.2 Rate Theory

In order to interpret experimental data, a theoretical framework is needed. Several papers assume that quartz dissolution rate is first order based on silicic acid (the dissolved form of silica). This has been experimentally verified up to 300°C in pure water with up to 10 mmol/L silica [4]. In the presence of foreign ions such as sodium or lead, however, this may not be the case due to competitive adsorption between silicic acid and the foreign cations at the silica surface.

Silica dissolution rate can, in its simplest form, be described as a function of the solid surface area (A), the fluid volume (V) and a forward rate constant k_f

$$\left(\frac{dc_{\mathrm{SiO2}}}{dt}\right)_{\mathrm{f}} = k_f \frac{A_{\mathrm{surf}}}{V_{\mathrm{fluid}}} \tag{1}$$

In an equilibrium situation, the forward (dissolution) and backward (precipitation) rates are equal, meaning that

$$K_{\mathrm{eq}} = \frac{k_f}{k_b} \tag{2}$$

where k_b is the backward rate constant. Such a relation is valid in the case of no nucleation only, i.e. when the rate of growth and dissolution of the same particle surface are equal. Silica dissolves as silicic acid according to

$$\mathrm{SiO_2} + 2\mathrm{H_2O} = \mathrm{H_4SiO_4} \quad , \quad K_{\mathrm{eq}} = \frac{a_{\mathrm{H_4SiO_4}}}{a_{\mathrm{SiO_2}} a_{\mathrm{H_2O}}^2} \tag{3}$$

For the case of pure silica, the solid silica activity is one. In (relatively) pure water the water activity can be further taken as one and $K_{\mathrm{eq}} = a^{\mathrm{eq}}_{\mathrm{H_4SiO_4}}$. This allows the backward rate constant to be expressed as a function of the forward one and the equilibrium dissolved silica concentration (note the negative sign since precipitation decreases dissolved silica while rate constants are kept positive)

$$\left(\frac{dc_{\mathrm{SiO2}}}{dt}\right)_{\mathrm{b}} = -k_b a_{\mathrm{H_4SiO_4}} \frac{A_{\mathrm{surf}}}{V_{\mathrm{fluid}}} = -\frac{k_f}{K_{\mathrm{eq}}} a_{\mathrm{H_4SiO_4}} \frac{A_{\mathrm{surf}}}{V_{\mathrm{fluid}}} \tag{4}$$

Furthermore, the net rate of change can (with unit activities for water and solid silica) be expressed as

$$\left(\frac{dc_{\mathrm{SiO2}}}{dt}\right)_{\mathrm{net}} = \left(\frac{dc_{\mathrm{SiO2}}}{dt}\right)_{\mathrm{f}} + \left(\frac{dc_{\mathrm{SiO2}}}{dt}\right)_{\mathrm{b}} = k_f \frac{A_{\mathrm{surf}}}{V_{\mathrm{fluid}}} \left(1 - \frac{a_{\mathrm{H_4SiO_4}}}{a^{\mathrm{eq}}_{\mathrm{H_4SiO_4}}}\right) \tag{5}$$

For systems with low levels of dissolved silica the net change equation, Eq. (5), reduces to the forward equation while for large supersaturation the limit goes to the backward equation. It is customary to further simplify rate equations by replacing activity with concentration. For dilute solutions with low ionic strength this is justified. Activities in Eq. (5) can also be replaced

with concentrations for non-ideal solutions when the equilibrium concentration is known for the electrolyte in question since activity coefficients (cf. $a = \gamma c$) cancel.

The above equations have been formulated using molar concentration and fluid volume. They may easily be recast using molal and fluid mass. Either way, the unit of the rate constant is $mol \cdot m^{-2} s^{-1}$. Formulations using mass of silica are also possible, then the rate constant must be formulated in terms of mass accordingly.

3.3 Experimental

Silica dissolution experiments were carried out in packed columns placed inside a furnace. In a typical experiment, 10 g of quartz (acid washed and calcined sea sand from Merck) was packed into a stainless-steel tube (270 mm length, 9.1 mm ID, 17.56 mL). A quartz fraction 125 < dp < 250 µm, obtained by sieving, was used in all experiments. The sieved powder was washed with tap water to remove fine grains. The pore volume was measured gravimetrically by flooding with water, giving roughly 50 vol% solids in the column. Filters were placed at both ends of the column to keep the solids in place. Sodium chloride (NaCl) was purchased from Merck.

A precision pump (Isco Teledyne) filled with the desired test fluid was connected to the column inlet, separated by a needle valve placed in the cold zone (outside the furnace). This pump provided system pressure and allowed flow-through experiments to be carried out with constant flow. The column outlet was connected to a condenser to lower the temperature while still pressurized, and the pressure was subsequently reduced through a pressure regulator taking in the cooled fluid. Fluid samples were collected using an automized collection unit (fraction collector). Samples were stored in plastic tubes and then analysed for silicon and sodium content using ICP-OES (Inductively Coupled Plasma Optical Emission spectroscopy). Note that samples were not diluted before storage. There was no sign of precipitation in the containers, and the fact that silica concentrations with significant supersaturation with respect to ambient temperature and pressure were measured suggests that precipitation during storage was not a significant issue. Rapid cooling to quench samples from precipitation is common practice in minerology. Note that silica concentration measured using spectroscopic methods (cf. molybdate test) may be more affected by storage. Long-term storage could lead to polymerisation (a precursor to precipitation) and such chains are not properly accounted for in the molybdate test. Preservation in acidic solution which is suggested by some authors is not recommended for silica samples. Since the solubility increases with increasing pH, it would be better to preserve samples in alkaline solution. The eluent was also regularly analysed for iron to monitor possible corrosion of the setup. Dissolved iron concentrations were typically several ppmw after a prolonged stagnant period of heating, but decreased to low and often non-measurable levels during sampling. Based on this it was concluded that corrosion of the equipment did not jeopardize the integrity of the setup. A sketch of the setup is shown in Figure 3.1.

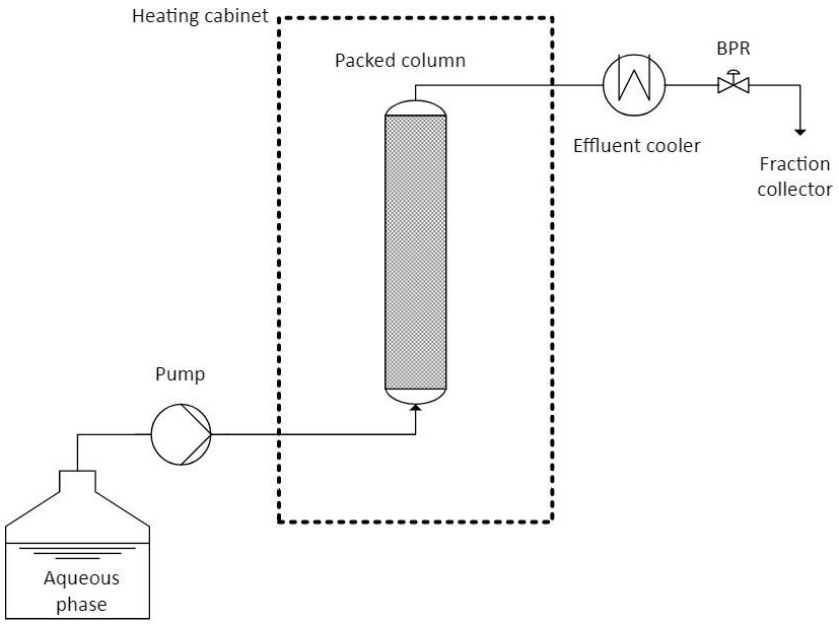

Figure 3.1: Sketch of the packed column setup.

Experiments were carried out using a model fluid of pure water with NaCl up to 30 g/L (ambient). Temperatures ranged from 300 to 400°C. Below the critical temperature, experiments were carried out at both side of the liquid-vapor pressure, meaning that experiments were carried out both for the gas phase and for the liquid phase. Above the critical temperature, pressures were selected to stay outside the two-phase envelope of the H_2O-NaCl binary system. Instead of taking samples exposed at different time intervals, experiments were carried out using variable flow rates. These had to be matched to the expected kinetics and varied from 0.02 to 10 mL/min depending on the temperature. An overview of kinetic experiments is given in Table 3.1. Experimental conditions are also indicated in the binary H_2O-NaCl phase diagram in Figure 3.2 below.

Table 3.1: Summary of experimental conditions.

Temperature °C	Pressure bar	NaCl g/L	State
300	75	0, 0.1, 1	Vapor
300	100	1	Liquid
350	150	1	Vapor
350	180	1, 5, 30	Liquid
380	240	1, 5, 30	Supercritical
400	290	1, 5, 30	Supercritical

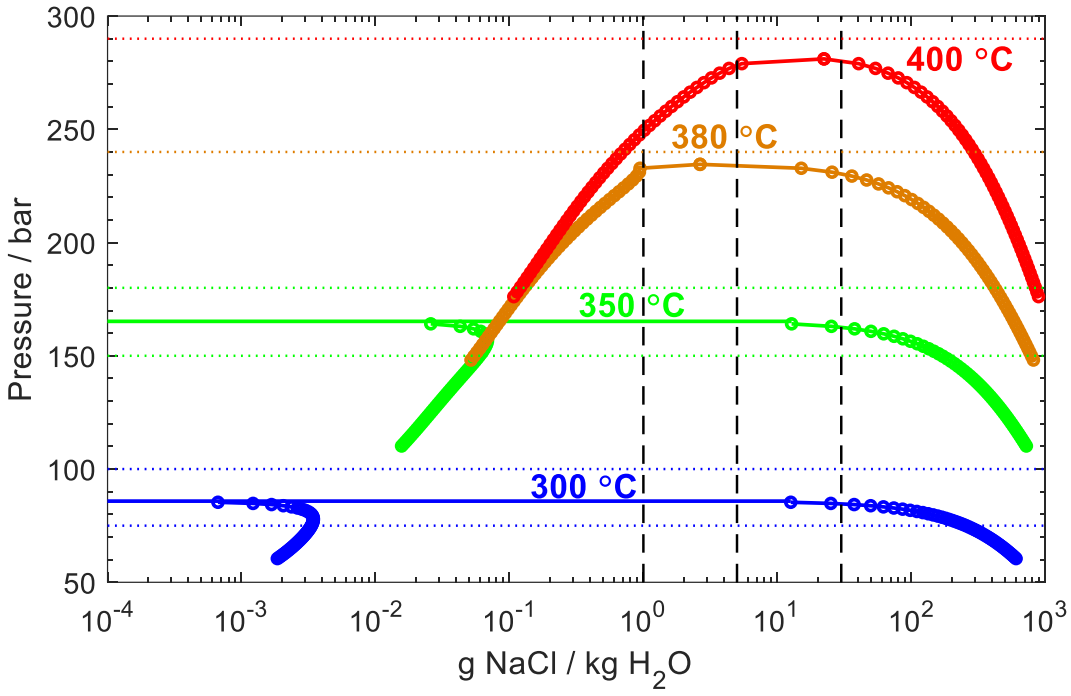

Figure 3.2: Binary phase diagram of the H_2O-NaCl system at different temperatures according to the model in Ref. [5]. Dotted horizontal lines indicate pressures studied in this work, while dashed black lines indicate salinity values studied.

3.4 Methods

3.4.1 Packed Bed Reactor

In order to analyse the results and rule out some possible artefacts, some calculations are carried out for the packed bed reactor system. For this purpose, the fluid is treated as single phase pure water flowing through a packed bed with 50% porosity. For each set of experimental conditions, temperature and density are assumed to be constant. Density and viscosity values are obtained using IAPWS-97 [6] and a single particle diameter of 127 µm is used, as obtained from the mean value in the particle size measurement. The Reynolds number (*Re*) and pressure drop per unit length (*dp*/*dz*) were then calculated for the upper and lower flow rates using the equations

$$Re = \frac{1}{1-\varepsilon}\frac{\rho D_p v}{\mu} \tag{6}$$

$$\frac{dp}{dz} = -\frac{v}{D_p}\left(\frac{1-\varepsilon}{\varepsilon^3}\right)\left[\frac{150(1-\varepsilon)\mu}{D_p} + 1.75\rho v\right] \tag{7}$$

where ρ is density, v is superficial velocity (i.e. volumetric flow divided by tube cross section), D_p is particle diameter, μ is dynamic viscosity and ε is porosity. For packed bed reactors laminar flow is typically defined as $Re < 10$ and turbulent flow for $Re > 1000$ with transitional flow in between. All experiments carried out in this work are towards the laminar end, with

the highest Reynolds number being 28, but most experiments had *Re* < 10. Hence, all experiments were treated as being in the laminar flow regime. The highest pressure-drop was calculated to be 167 mbar/m. For a 0.27 m column with a total pressure above 300 bar, this is taken as negligible and the volumetric flow rate is treated as constant throughout the column. Comparing different temperature and pressure experiments, the Reynolds number varies only inversely with viscosity since the product ρv (i.e. the mass flux) is constant when the flow rate is controlled using volumetric rate at room temperature.

A mass balance for a flow-through experiment can be found in literature written in molar concentrations, e.g. Ref. [7]. For fairly incompressible fluids this is intuitive, but in order to avoid confusion when dealing with compressible water the equation is here formulated in terms of a concentration, *c*, with units mol/kg H_2O, and a mass flow rate, $\dot{m}$.

$$\frac{dc}{dt} = r\frac{A_{\text{surf}}}{m_{\text{H2O}}} - \frac{\dot{m}}{m_{\text{H2O}}}(c_{\text{out}} - c_{\text{in}}) \tag{8}$$

In this equation, *r* is the dissolution rate, A_{surf} is the particle surface area (i.e. here BET area times mass of particles), m_{H2O} is the mass of water in the reactor and c_{out} and c_{in} are outlet and inlet concentrations of dissolved silica, respectively.

Outlet concentrations should be sampled at steady state conditions, cf. the discussion above and Figure 3.4, where $dc/dt = 0$ and the mass balance simplifies to

$$r = \frac{\dot{m}}{A_{\text{surf}}} c_{\text{out}} \tag{9}$$

when also considering that $c_{\text{in}} = 0$. Equations (8) and (9) could also be formulated with a time variable, using that mean residence time is $\tau = m_{\text{H2O}}/\dot{m}$.

3.4.2 Fluid Data Treatment

A series of solubility experiments was always started from a pressurized column at the desired temperature, meaning that the system is filled with an equilibrium fluid. The initial plan was to first extract two pore volumes to extract the equilibrated fluid and have a front of fresh fluid entering the column. Then, four samples of one pore volume each would be analysed for silica content. It was believed that the four last samples would (in theory) have the same concentration, and that averaging over four samples would even out random errors and also give the possibility to discard obvious outliers. This was all based on tritium test of the setup with tracer response shown in Figure 3.3.

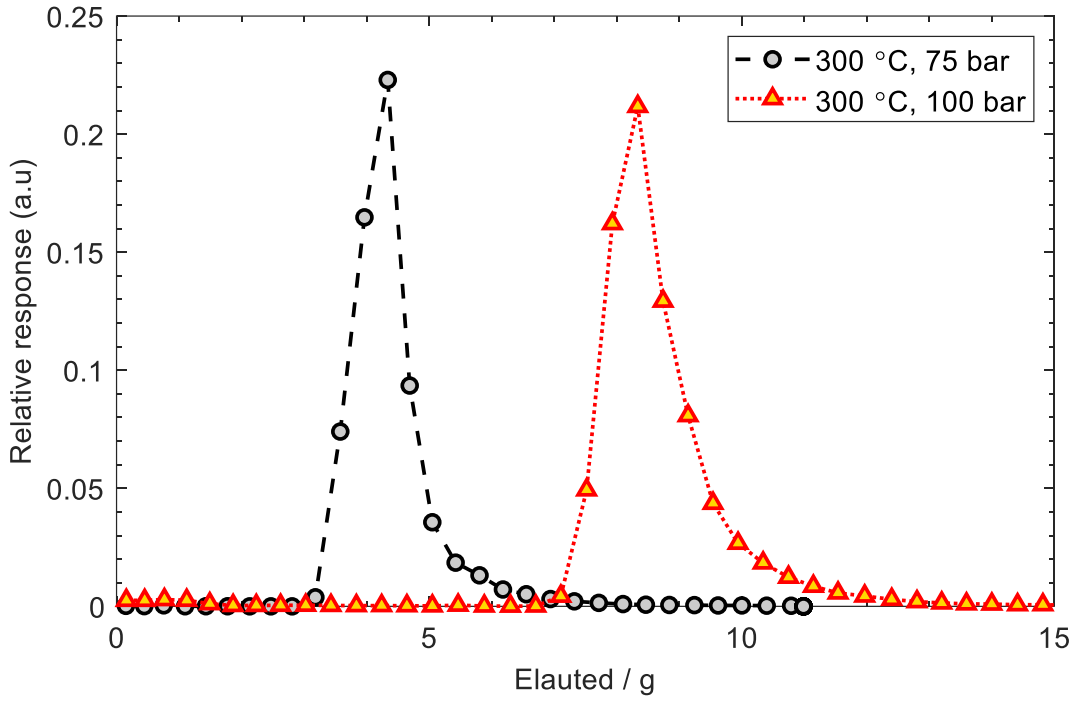

Figure 3.3: Tritiated water test of a packed column at 300°C at both sides of the vapor-liquid coexistence curve

Upon analysing data, however, it became clear that data did not follow such an ideal behaviour. Some sets had a fairly random value around an average, while others showed more exponential decay towards a stable value. An example is shown in Figure 3.4 where Si concentrations of all samples taken at 380°C and 240 bar are plotted against sample number. Exponential decay curves, cf. blue and magenta curves in Figure 3.4, are reported as fit values as time goes to infinity ($t \rightarrow \infty$) after disregarding the first sample which is low attributed to start-up effects. The green curve, although showing an overall decrease with sample number, is treated as randomly scattered and simply reported as average value after discarding the first two as initially intended. For the cyan curve it is not clear how to extract the most representative value, but it is reported here as an exponential fit of the last five samples. The red curve shows a decreasing trend for samples 3—6 from which a steady state value cannot be estimated. Therefore, this data set is excluded from further analysis. Remarks regarding how each data set was treated (i.e. how the steady state value was obtained) are included in the data set [8].

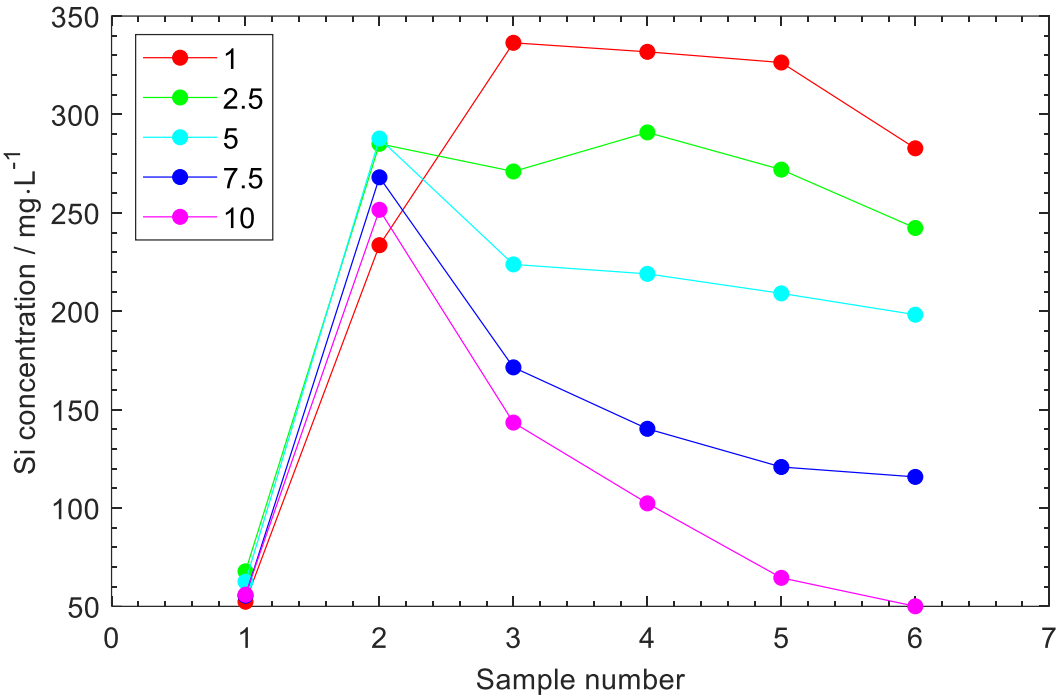

Figure 3.4: All Si samples analysed for the experiment at 380°C and 240 bar (run 45-49). The legend shows flow rates in mL·min^{-1}. Sample number along the x-axis is equivalent to cumulative volume in cL, since each sample was 10 mL.

3.5 Results and Discussion

3.5.1 Characterisation of SiO_2

For the purpose of these experiments, the silica surface area is considered to be constant throughout the duration of an experimental series. This assumption is supported by scanning electron microscopy (SEM) images taken before and after exposure to the test fluid, cf. Figure 3.5. No significant change in size was found. The BET surface area of the quartz fraction was found to be 0.69 m^2/g and the mean particle size as obtained using light scattering was 127 µm.

As with all natural (mineral) samples, some impurities are expected. Although the quartz as purchased was purified by acid wash and calcinated, the colour indicated some impurities were still present. Pure quartz is expected to be white, while this batch had a grey/brown tint. X-ray diffraction confirmed that the particles were mainly quartz, with some minor unidentified impurity peaks (cf. REFLECT D2.3).

Energy dispersive X-ray spectroscopy (EDS) mapping of as-purchased quartz show mainly particles of Si and O with minor Al as an impurity. Also present are some particles rich in Al and K, in addition to Si and O, resulting in an average stoichiometry of $KAlSi_4O_{10}$ (cations were included as rounded numbers and O added to maintain charge balance). Minor Ti and Fe impurities were also detected in EDS.

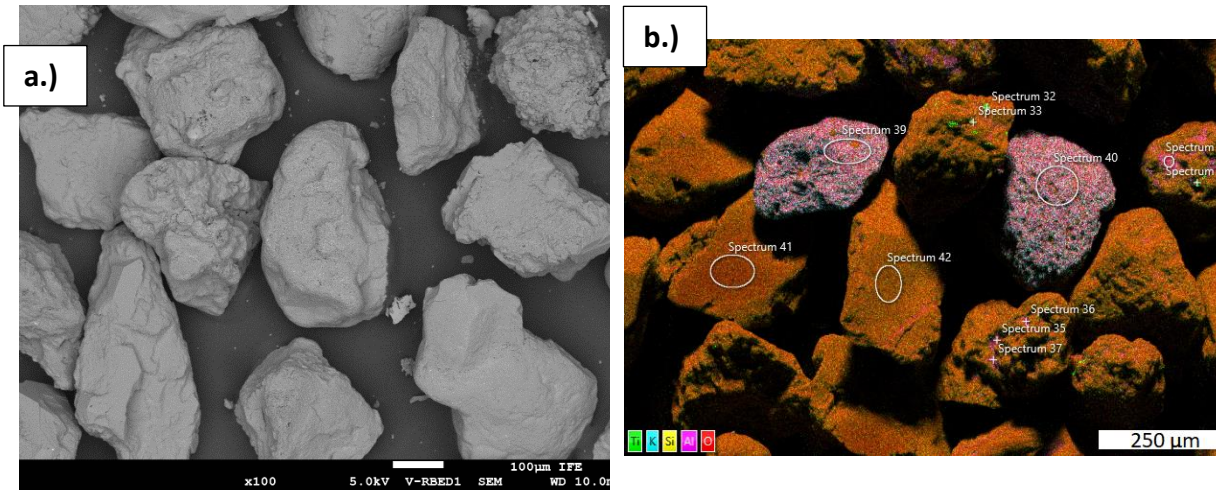

Figure 3.5: Backscatter SEM image (a) and EDS map (b) of as-purchased quartz particles

3.5.2 Dissolution Rates

At 300°C and 75 bar, only measurements using an ambient flow rate of 0.05 mL/min are included. Here, since the first two samples were discarded without Si analysis, no equilibrium value is available. Also note that samples were not analysed for Na, meaning that the possibility of two-phase sampling (see below under description of 350°C, 150 bar results) cannot be ruled out. Nevertheless, rate constants are calculated assuming that only vapor phase was sampled. For the current set of experiments, all steady state values were obtained using decay fits (cf. Figure 3.4). In the current rate constant calculations, some considerations regarding the equilibrium solubility used in Eq. (4) are needed, since measured outlet concentrations are larger than those predicted by the model [9]. Therefore, it is unlikely that our measurements were far enough from equilibrium for the *Q*/*K* term not to be of importance. Experimental data in open literature tend to have larger solubility values than those predicted. The most extensive data set in vapor-like water is Ref. [10] (data available in an English publication [11]), which has almost 3 times larger value at 300°C and 49 bar. This ratio is assumed to hold also at 75 bar, and an equilibrium solubility of 0.003 g SiO_2/kg H_2O is used.

For the data set at 300°C and 100 bar, a three-point average of the last three samples at each flow rate was used. For these measurements, the first two samples (cf. Figure 3.4) where discarded without analysing, meaning that an estimate of the equilibrium value cannot be obtained. Measured values for all flow rates tested are around 0.06 g SiO_2/kg H_2O, which is an order of magnitude lower than model reference data [9]. This, and the fact that solubility values for this silica batch is larger than the quartz model (cf. REFLECT D2.3) indicates that the current measurements were far from equilibrium. This means that $a_{H_4SiO_4}/a^{eq}_{H_4SiO_4}$ in Eq. (5) is small and the exact value of the equilibrium value is of less importance for the calculated forward reaction rate constant. In the current work a value of 0.6075 g SiO_2/kg H_2O was used for the equilibrium concentration.

Conversion to a backward rate constant through Eq. (2), however, is directly proportional to the equilibrium solubility. Due to the ambiguity in equilibrium constants (our samples generally show larger solubility than model quartz, the quartz model appears to

underestimate experimental literature values at low fluid density), both dissolution rate constants - as obtained from the measurements – and calculated precipitation rate constants are reported along with the silica solubility used in the conversion.

For the series of experiments at 350°C and 150 bar only results of experiments with reasonable Na values are included. For example, too high Na values with respect to literature NaCl solubility in a gas-phase experiments would suggest at least partly liquid sampling and hence lead to silica values not representative for the particular test. Several experiment series at different flow rates had to be discarded due to experimental artefacts. A solution oversaturated with NaCl was flooded through the system, i.e. a 1 g/L solution where the solubility of NaCl in vapor at the experimental conditions is 0.06 g NaCl/kg H_2O. As can be seen from the binary phase diagram, shown in Figure 3.2, a liquid brine with high NaCl solubility would form at conditions located within the phase envelope. This brine is expected to cover quartz surfaces and lead to a higher silica solubility. If such droplets are carried over to the sampling line, the measured sample would have a concentration equal to the weighted average of liquid and vapor concentrations ($m_{\mathrm{out}} = X_{\mathrm{liq}} m_{\mathrm{liq}} + X_{\mathrm{vap}} m_{\mathrm{vap}}$). This would lead to unreasonably large concentrations of both Si and Na in the ICP-analysis, and this is exactly what was measured. From a sodium mass balance and binary phase behaviour, it is possible to calculate the fraction of vapor and liquid in the sample, but since silica concentrations in both phases are unknown the system cannot be solved. For the two data sets that are treated, the same considerations applies as for 300°C and 100 bar: No experimental equilibrium value is available, but the low silica values measured (around 0.001 g SiO_2/kg H_2O cf. a model value one order of magnitude larger) leads to the assumption that they were taken far from equilibrium and that the exact solubility is not crucial for the calculated forward rate constant. In order to be somewhat consistent with the choice for 300°C and 70 bar, a value 3 times the model (0.036 g SiO_2/kg H_2O) was used in this work. Future experiments should not use salt concentrations causing two-phase behaviour, unless a proper liquid trap is included in the experimental setup.

As a side result, the NaCl solubility in vapor-like water at 350°C and 150 bar was found to be 0.022 ± 0.003 g NaCl/kg H_2O based on in total eight samples with reasonable Na values. This value is lower than both the model behind Figure 3.2, Ref. [5], and the experimental value of 0.033 g NaCl/kg H_2O [12].

Experiments at 350°C and 180 bar are shown as outlet concentration, as extracted using the procedures outlined in Section 3.4.2, plotted against flow rate in Figure 3.6. ICP measurements included also Na (not shown), which were all in a reasonable range. Some flow rate series still had to be discarded since a steady state value could not be obtained. Measured outlet concentrations at low flow rates were larger than model values, but the agreement was much better than for the low-pressure vapor like experiments; our maximum steady state outlet concentration was 1.06-1.15 times larger than the model. Hence the maximum outlet concentration was taken as the equilibrium value for each salinity. As explained above, the further away from equilibrium (i.e. the faster the flow rate), the less effect the used equilibrium value has for rate calculations. It should be emphasized that the point at 1 mL/min for 350-180-5 stands out as being too high. This was the first experiment after replacing the column, and it was concluded that the high solubility was due to highly reactive silica surface that dissolved and was therefore not observed in subsequent measurements. Since

solubilities in this work obtained from measurements are close to the model, a model solubility of 0.72 g SiO_2/kg H_2O was used for this particular set.

Reactivity of silica surfaces depend on surface conditions. In a microscopic model [13] the dissolution rate was expressed in terms of spacing and height of reactive steps. Comprehensive pre-treatment procedures has been used on silica samples to remove highly reactive sites, but still observed remarkable agreement with results from other laboratories employing different treatments was observed [14]. In our experiments, the pre-treatment was (implicitly) carried out *in situ*. The column was heated to target temperature and left at least overnight for equilibration before the first test when using a freshly prepared column. It is believed that this procedure removed the highly reactive sites. This was only observed in the first flow rate with a freshly packed column after 350-180-5 which was omitted from further analysis. No other such outliers could be observed in the experiments.

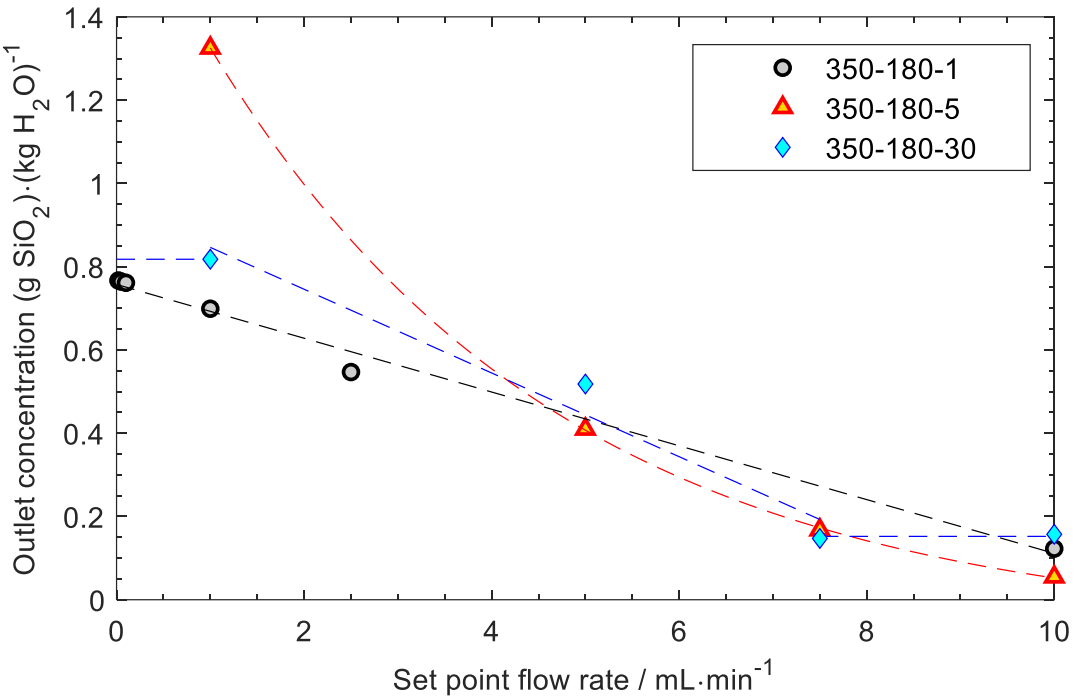

Figure 3.6: Outlet total silica concentration as a function of flow rate for experiments at 350°C, 180 bar and (ambient) NaCl concentrations of 1, 5 and 30 g/L as indicated in the legend. Dashed lines are included as guides to the eye.

Series at 380°C and 240 bar and 400°C and 290 bar were treated similarly as 350°C and 180 bar. Results showing outlet concentration vs flowrate are shown in Figure 3.7 and Figure 3.8. Steady state values for each flow rate were obtained using exponential fits where a decaying trend was observed, and from an average where points appeared to have reached a plateau. The maximum outlet concentration was taken as the equilibrium value for each combination of temperature, pressure and salinity. It is noted that solubility values extracted from this work are 1.4—2.1 times larger than predicted by the model at 380°C and 1.8—2.7 times larger at 400°C. The experiment with 10 mL/min at 400°C and 290 bar with 30 g/L NaCl had to be discarded altogether due to experimental issues. The pump was not able to

maintain the pressure, resulting in highly pulsating flow. This was probably caused by a slug-flow, a flow regime known from the oil and gas industry. Slug flow can occur in two-phase systems when there is gas and liquid flow rates within a certain range. There are several possible explanations why a two-phase situation occurred in this particular experiment. For example, local clogging of pores could lead to increased pressure drop, bringing the fluid into the two-phase envelope (cf. Figure 3.2). Also, insufficient time to heat the fluid on its way into the column may cause the phase change front to enter the column. A future mitigation strategy would be to have a longer heating coil into the column to ensure sufficient heating and to use a shorter column for the higher temperatures. A shorter column will decrease the particle surface area and hence allow lower flow rates for the same conversion ($r \propto \dot{m}/A_{\mathrm{surf}}$).

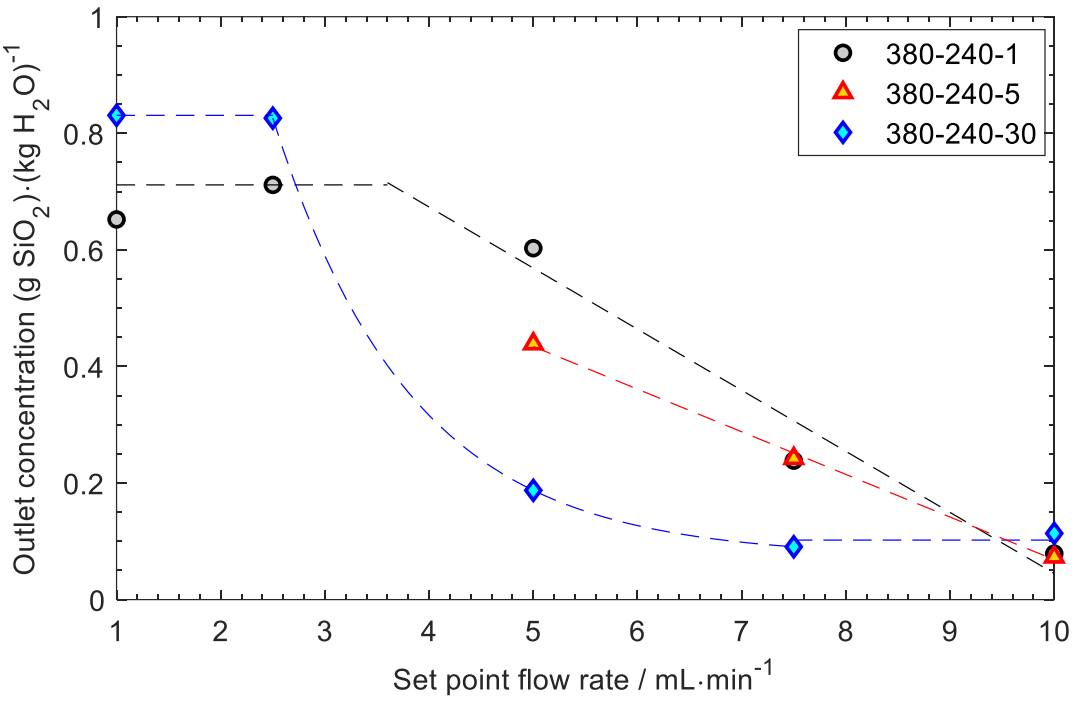

Figure 3.7: Outlet concentration as a function of flow rate for experiments at 380°C, 240 bar and (ambient) NaCl concentrations of 1, 5 and 30 g/L as indicated in the legend. Dashed lines are included as guides to the eye.

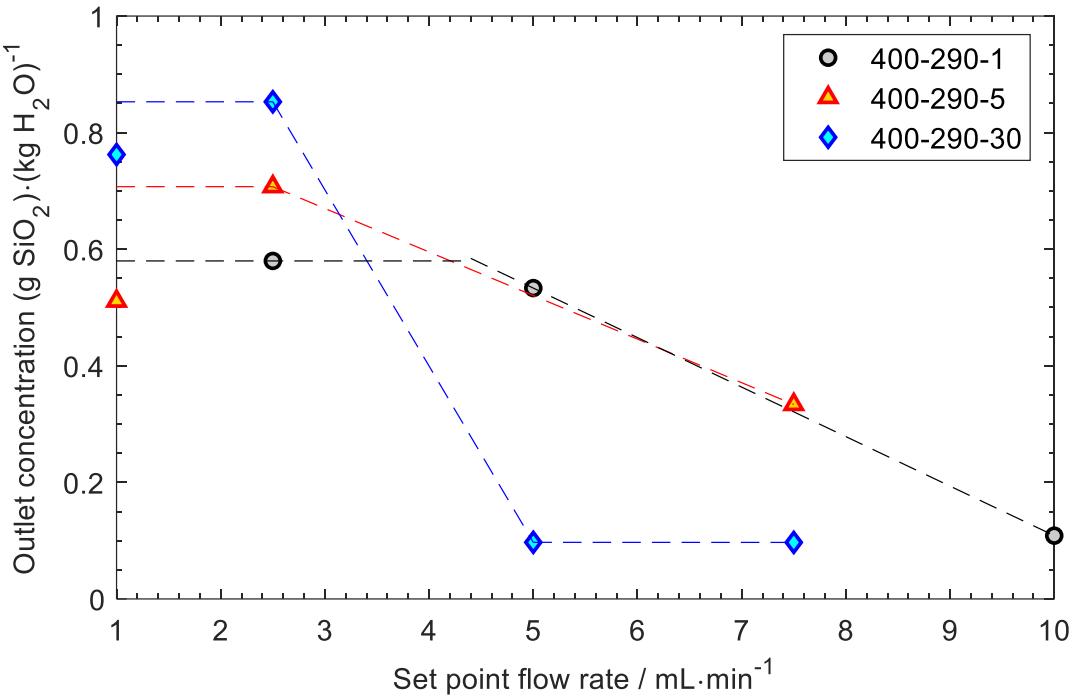

Figure 3.8: Outlet concentration as a function of flow rate for experiments at 400°C, 290 bar and (ambient) NaCl concentrations of 1, 5 and 30 g/L as indicated in the legend. Dashed lines are included as guides to the eye.

A certain temperature drop in the fluid during sampling at high flow rates may have influenced the results. Initial tests at (300 and 350°C) were carried out with a thermocouple inserted into the outlet of the packed column. No temperature drop could be observed during the continuous flow experiments (manual readings, no digital recording available). The inserted thermocouple proved a vulnerable spot causing a leak, and was therefore removed in further testing at higher temperature. Hence, the possibility of a temperature drop at the higher flow rates cannot be ruled out and it´s possible consequences are worth some consideration.

Figure 3.9 shows model quartz solubility in pure water as a function of temperature for the isobars studied in this work. Grey stars mark the setpoint temperature along each isobar. For the 75 and 150 bar experiments, i.e. measurements carried out sampling gas phase, a temperature decrease would lead to increased solubility. The increase would be significant if condensation took place due to crossing of the liquid-vapor phase boundary. This follows directly from the abrupt density change associated with the phase transition. Experiments carried out above the liquid-vapor coexistence curve, cf. 100 and 180 bar, were both close to the maximum solubility along the isobars. For the 100 bar experiment one would expect reduced solubility with decreasing temperature, while the one at 180 bar was close to a maximum and a temperature drop would initially result in increased solubility followed by a decrease upon further reducing the temperature. Qualitatively, the trend for 240 and 290 bar experiments are the same as for the one at 180 bar. However, it is unlikely that the temperature would drop sufficiently to get a lower solubility than the starting point. Hence, an increased solubility would be expected in practice.

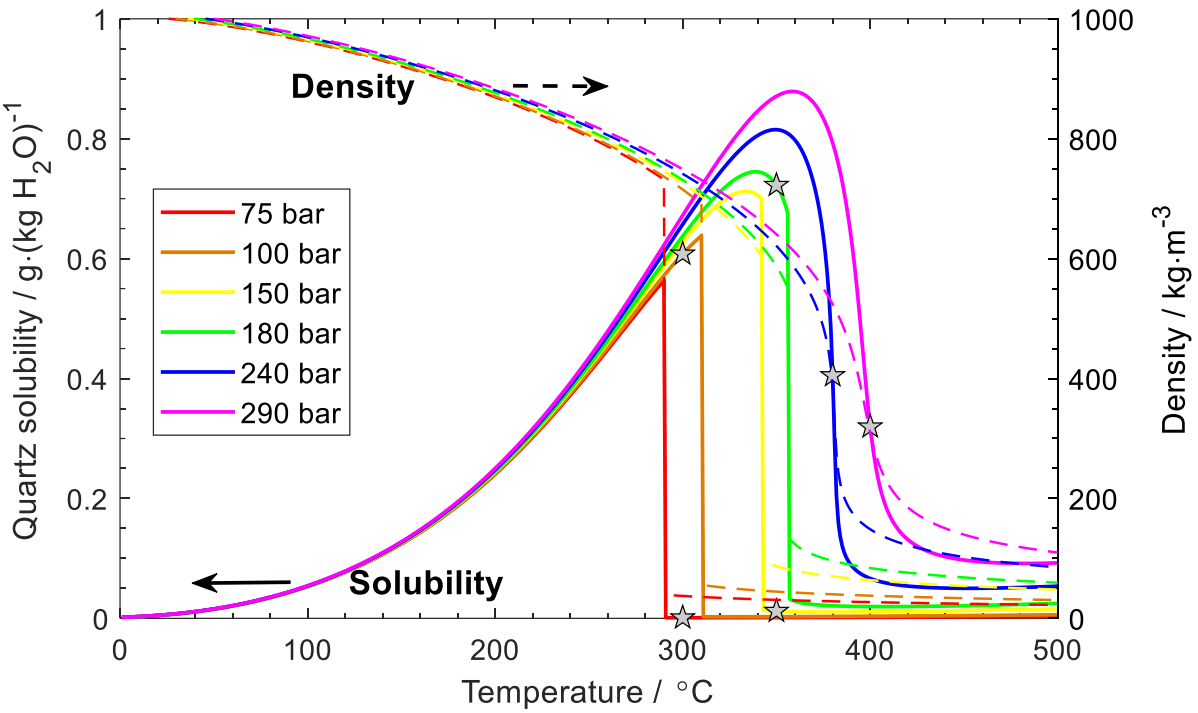

Figure 3.9: Quartz solubility in pure water according to the model in Ref. [9] (solid lines, left axis). Included are also water density (dashed lines, right axis) according to Ref. [6].

Since the high flow rate tests are somewhat away from equilibrium, the possible effect of a temperature drop during sampling cannot be quantified. The effect, however, would in practice manifest itself as an increased outlet silica concentration with increasing flow rate. Note that a constant outlet temperature would not alone guarantee that experiments at different flow rates are directly comparable, since the temperature profile (cf. effective temperature) inside the column may still be different. Future setups should include a thermocouple before the column inlet to ensure that the fluid has reached the desired temperature before meeting the dissolving particles.

In light of the above discussion, a critical selection of data points to be included in rate constant figures was carried out while keeping all calculated rate constants available in the data set [8]. When possible, points far away from equilibrium (i.e. high flow rate) were chosen as to not be overly affected by the equilibrium concentration, cf. Eq. (5). However, points showing sign of decreased outlet temperature by having increased solubility with increasing flow rate were omitted. For example, for the 400°C and 290 bar series in Figure 3.8, the point at 5 mL/min was chosen. The resulting dissolution rate constants are shown in Figure 3.10 and precipitation rate constants in Figure 3.11, where k_- is calculated using the relation in Eq. (10), where the molar fraction of water (X) is used for the water activity

$$k_- = k_+ \frac{X_{\mathrm{H_2O}}^2}{c_{\mathrm{H_4SiO_4}}^{\mathrm{eq}}} \qquad (10)$$

Both figures show qualitatively the same trend with temperature and salinity. There is a significant increase from 300 to 350°C, but then there is an ambiguous trend when further

increasing the temperature to 400°C. The set with 5 g/L NaCl shows a steady increase with increasing temperature, while the one with 30 g/L drops from 350 to 400°C. Data for 1 g/L NaCl shows a small increase from 350 to 380 before decreasing towards 400°C. There is no clear effect of the salt content within the range tested. Experiments carried out at low pressure with gas-like systems show significantly lower rate constants.

Dissolution rate constants in open literature [2] show a clear increase with increasing temperature. The data set at the higher temperatures are from a study of fluids with high density above 1000 bar and not directly comparable, but the data points by Kithara are from similar densities and show dissolution rate constants around $10^{-4.5}$ referred to the geometric surface area while BET area is used in the current work. Ref. [2] compared BET and geometric area for one type of sand and found that the former was roughly 7 times larger. Even if this factor is incorporated, the current work show rate constants more than an order of magnitude lower than literature reports at 400°C ($5 \cdot 10^{-6}$ vs 10^{-7} mol/m^{2}s). This is somewhat surprising considering that most literature values are for pure water, while most of the points in the current work are in the presence of NaCl. Dissolution rates have been shown to increase in the presence of alkali cations in the range 100-300°C, where minor additions (0.05 molal) increased the rate substantially (33 times) [15]. One possible explanation is that the effect of cations decreases with increasing temperature. Such a deceasing trend with increasing temperature has been reported for both quartz and amorphous silica for the precipitation reaction [16].

pH also has an effect on the rate of silica dissolution and precipitation rates. Dissolution rates have been shown to be pH dependent with a minimum around PZC (point of zero charge) (pH = 2) and the rate increases by several (3) orders of magnitude from pH 3 to pH 7. The presence of NaCl could affect the pH through hydrolysis ($NaCl + H_2O = NaOH + HCl$), but the extent of this reaction is expected to be small at the conditions investigated.

Silica samples used in this work contained some Al according to the EDS results. The presence of Al^{3+} has been reported to decrease silica dissolution rates significantly [16], albeit the effect at high temperature is less known.

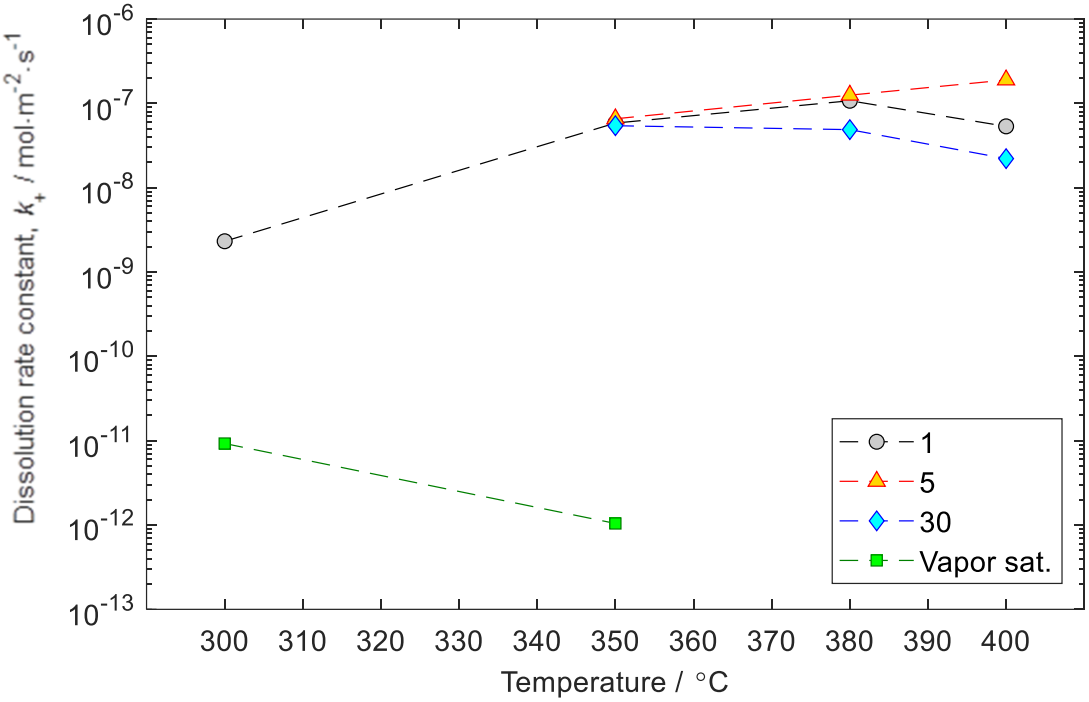

Figure 3.10: Selected dissolution rate constants as a function of temperature for different NaCl levels as indicated in the legend. The low-pressure experiments (green squares) were saturated with NaCl.

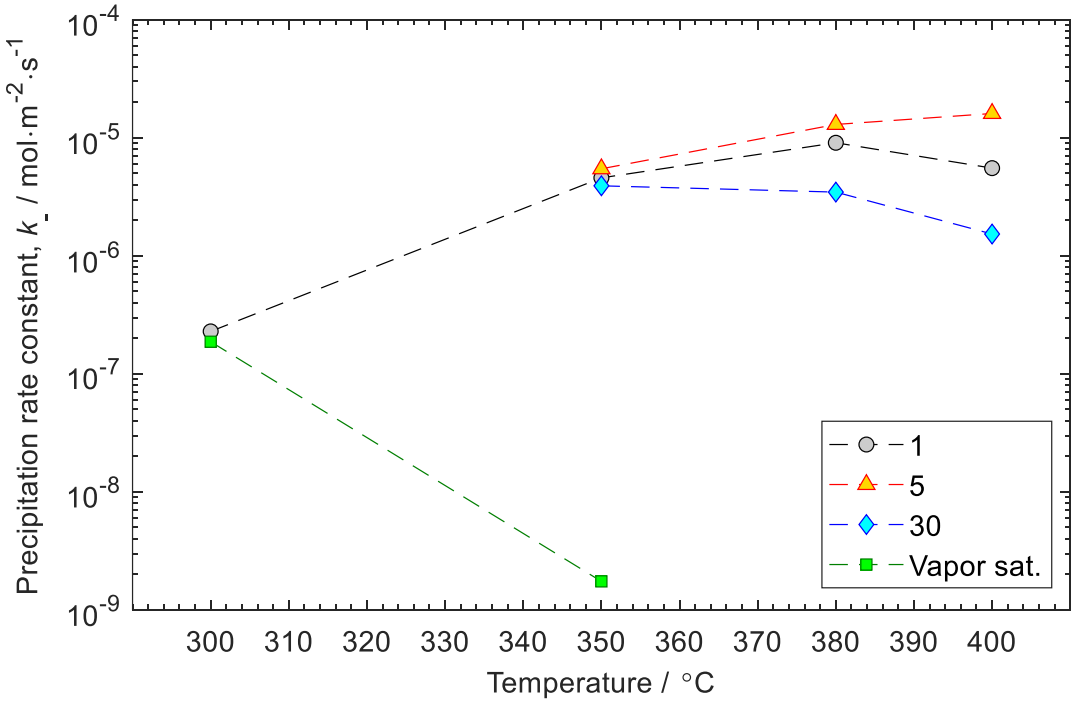

Figure 3.11: Selected precipitation rate constants (as obtained from dissolution experiments) as a function of temperature for different NaCl levels as indicated in the legend. The low-pressure experiments (green squares) were saturated with NaCl.

3.6 Conclusion

Quartz dissolution experiments has been carried out in a packed column setup using different flow rates to obtain kinetic information. Conditions ranged from 300 to 400°C with pressures from 75 to 290 bar, covering both gaseous, liquid and supercritical water. The effect of salinity was studied by varying the NaCl concentration from 1 to 30 g/L (referred to ambient water). Rate constants were then converted to precipitation rate constants using theory described in open literature.

Dissolution rate constants were in the range 10^{-9} to 10^{-7} mol/m^{2}s for liquid and supercritical water and 10^{-12} to 10^{-11} mol/m^{2}s for vapor-like water. Calculated precipitation rate constants were two orders of magnitude larger for liquid and supercritical and 3—4 orders of magnitude larger for gaseous water. The qualitative trends are similar for both precipitation and dissolution rates: There is a significant increase from 300 to 350°C, while from 350 to 400°C the temperature effect is small. Above 350°C the effect of cations (NaCl) is small.

Rate constants found in this work are lower than comparable literature results. It is believed that this is due to the presence of Al in the quartz samples.

3.7 References

1. J. D. Rimstidt and H. L. Barnes, *Geochimica et Cosmochimica Acta*, *The kinetics of silica-water reactions*, **44**, 1683 (1980).

2. J. W. Tester, W. G. Worley, B. A. Robinson, C. O. Grigsby and J. L. Feerer, *Geochimica et Cosmochimica Acta*, *Correlating quartz dissolution kinetics in pure water from 25 to 625°C*, **58**, 2407 (1994).

3. C. Dixit, M.-L. Bernard, B. Sanjuan, L. André and S. Gaspard, *Chemical Geology*, *Experimental study on the kinetics of silica polymerisation during cooling of the Bouillante geothermal fluid (Guadeloupe, French West Indies)*, **442**, 97 (2016).

4. G. Berger, E. Cadore, J. Schott and P. M. Dove, *Geochimica et Cosmochimica Acta*, *Dissolution rate of quartz in lead and sodium electrolyte solutions between 25 and 300°C: Effect of the nature of surface complexes and reaction affinity*, **58**, 541 (1994).

5. T. Driesner and C. A. Heinrich, *Geochimica et Cosmochimica Acta*, *The system H2O–NaCl. Part I: Correlation formulae for phase relations in temperature–pressure–composition space from 0 to 1000°C, 0 to 5000bar, and 0 to 1 XNaCl*, **71**, 4880 (2007).

6. W. Wagner, J. R. Cooper, A. Dittmann, J. Kijima, H.-J. Kretzschmar, A. Kruse, R. Mareš̆, K. Oguchi, H. Sato, I. Sto¨cker, O. S̆ifner, Y. Takaishi, I. Tanishita, J. Tru¨benbach and T. Willkommen, *Journal of Engineering for Gas Turbines and Power*, *The IAPWS Industrial Formulation 1997 for the Thermodynamic Properties of Water and Steam*, **122**, 150 (2000).

7. J. Cama, C. Ayora and A. C. Lasaga, *Geochimica et Cosmochimica Acta*, *The deviation-from-equilibrium effect on dissolution rate and on apparent variations in activation energy*, **63**, 2481 (1999).

8. M. Tjelta and S. O. Viig, *Silica dissolution and precipitation kinetics in hot getothermal conditions*, DOI:10.5281/zenodo.8341449 (2023).

9. N. N. Akinfiev and L. W. Diamond, *Geochimica et Cosmochimica Acta*, *A simple predictive model of quartz solubility in water–salt–CO2 systems at temperatures up to 1000°C and pressures up to 1000MPa*, **73**, 1597 (2009).

10. H. G. Heitmann, *Siemens - Schubertwerke Akg.*, *Die Loslichkeit von Kieselsaure in Wasser and Wasserdampf Sovie ein Einfluss auf Turbinenrerkiesselungen*, 163 (1963).

11. H. Allan, Evaluation and Correlation of Steam Solubility Data for Salts and Minerals of Interest in the Power Industry, in, - 1387, National Institute of Standards and Technology, Gaithersburg, MD (1997).

12. J. L. Bischoff and R. J. Rosenbauer, *Geochimica et Cosmochimica Acta*, *Liquid-vapor relations in the critical region of the system NaCl-H2O from 380 to 415°C: A refined determination of the critical point and two-phase boundary of seawater*, **52**, 2121 (1988).

13. P. M. Dove, N. Han and J. J. De Yoreo, *Proceedings of the National Academy of Sciences*, *Mechanisms of classical crystal growth theory explain quartz and silicate dissolution behavior*, **102**, 15357 (2005).

14. J. P. Icenhower and P. M. Dove, *Geochimica et Cosmochimica Acta*, *The dissolution kinetics of amorphous silica into sodium chloride solutions: effects of temperature and ionic strength*, **64**, 4193 (2000).

15. D. A. Crerar and P. M. Dove, *Chemical Geology*, *Kinetics of quartz dissolution in electrolyte solutions using a hydrothermal mixed flow reactor*, **84**, 301 (1990).

16. P. M. Dove and J. D. Rimstidt, *Reviews in Mineralogy & Geochemistry*, *Silica-water interactions*, **29**, 259 (1994)

4 Dissolution and Precipitation of Silica in a Sodium Chloride Solution with Conductometric Monitoring

Juliane Kummerow
Helmholtz Centre Potsdam – GFZ German Research Centre for Geosciences, Germany

4.1 Objectives

Mineral scaling is one of the biggest obstacles to the economically efficient use of geothermal energy, as it often leads to costly maintenance of both underground and above ground installations such as production and injection wells, pumps and heat exchangers (e.g. Wanner et al., 2017, Köhl et al., 2020). Geothermal fluids usually contain a variety of dissolved components such as salts, minerals and gases. However, changes in pressure and temperature during fluid production in a geothermal plant disturb the hydrochemical equilibria and can lead to precipitation of minerals due to supersaturation. This can subsequently significantly reduce the flow rates of the geothermal system and thus increase economic risk (e.g. Atkinson et al., 1991).

Silica precipitation is the primary obstacle when utilising high-enthalpy fluids for heat and power production, as the amount of dissolved silica increases with fluid temperature (e.g. Bouillante/ Guadeloupe: 600 mg/L; Hellisheidi/ Iceland: 800 mg/L) and can contain even more than 1000 mg/L SiO_2 (Dixit et al., 2016, 2019; van den Heuvel, 2018). In order to better predict the scaling behaviour of high-enthalpy geothermal fluids in geotechnical installations, new solubility and kinetic experiments were performed in the temperature range 100—495°C at 310 bar.

4.2 Experiments

4.2.1 Experimental Set-Up

Quartz solubility experiments at GFZ were carried out in a flow-through-cell that consists of a stainless steel pressure tube of 1 m length that is horizontally installed in a large tubular furnace (Figure 4.1). To avoid corrosion the pressure tube is lined with a corundum pipe with an inner diameter of 5 mm. A pair of current and potential electrodes made of platinum wires glued into corundum capillaries (outer diameter 4.6 mm) protrude into the set-up from each end of the corundum tube. Using these electrodes the reaction process in the reaction chamber can be monitored conductometrically *in situ*. The reaction chamber is the 14 cm long space between the two electrodes into which the quartz material was introduced. In addition, one of the electrodes is equipped with a Pt/Pt-Rh thermocouple for direct temperature control in the reaction chamber. Below supercritical conditions and at constant flow rate, temperatures in the reaction chamber are constant at ± 0.2°C. Above the critical point temperature fluctuations of up to ± 0.3°C within milliseconds were observed, possibly caused by flow perturbations. For more details see Kummerow et al. (2020).

An HPLC pump was used at the up-stream side for injecting the test fluid into the reaction chamber at a defined flow rate, while a high-accuracy metering pump (Vindum VP-12K) at the down-stream side maintained a constant fluid pressure. To avoid silica-enriched fluid in the

downstream pump, in most tests the percolated fluid was collected in a high-pressure tube with a floating piston (media separator/ dead volume = 0.043 cm^3) until the fluid sample was taken. The media separator was emptied and the fluid samples taken by slightly opening a spring-loaded pressure relief valve on the downstream side. In the primary layout used in the very first experiment however, the fluid was allowed to drip off directly at a pressure relief valve, where it was collected for ICP-OES analysis.

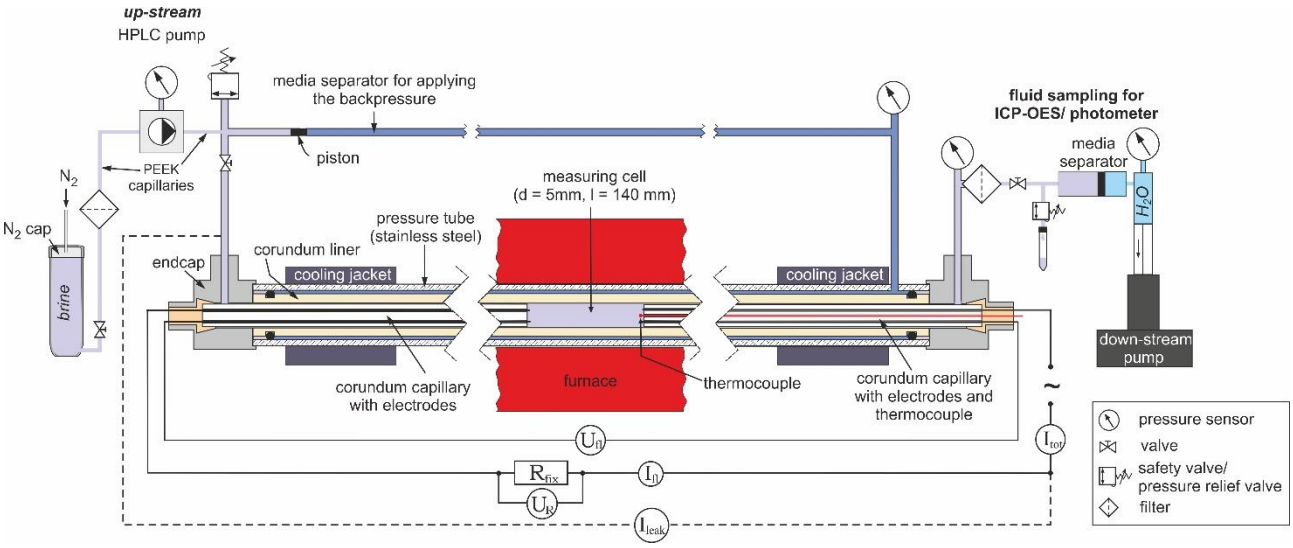

Figure 4.1. Schematic overview of the flow-through cell used for silica dissolution experiments.

4.2.2 Materials

Due to the horizontal positioning of the set-up, loose sand samples could not be handled and thus, small rock cores with a diameter of 4 mm and 6 to 7 cm length in total (m = 2 - 2.6 g) were prepared from a quartzite and the weakly consolidated Fontainebleau sandstone respectively, which is a pure quartz sandstone with a mean grain size of 265 µm and a porosity of 17.6% (see Figure 4.2 andFigure 4.3, Table 4.1). Before being used for the tests, the material was washed with 10% HCl for 60 seconds, subsequently cleaned with bi-deionised water and dried in a vacuum furnace.

Solubilities were tested in a 2.5 wt% sodium chloride solution that was prepared from high purity NaCl (Merck) and bi-deionised water. At the given volume of the reaction chamber of.75 cm^3 and of a sample volume of 0.8 cm^3 the fluid volume in the reaction chamber was about 1.95 cm^3.

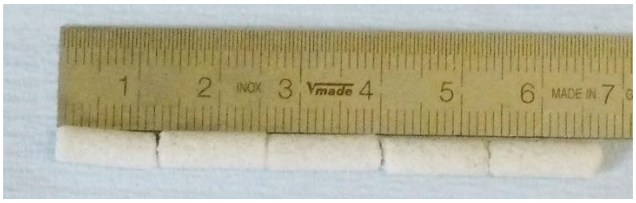

Figure 4.2. The prepared sandstone cores used in the experiments.

Table 4.1. EDX analysis of Fontainebleau quartz grains. Points of analysis correspond with numbers shown in Figure 4.3

Point of analysis	Si	O	Fe
001	44.52	55.48	0.00
002	45.29	54.71	0.00
003	49.41	50.49	0.10
004	46.90	53.10	0.00
005	45.42	54.58	0.00
Average	**46.31**	**53.67**	**0.02**

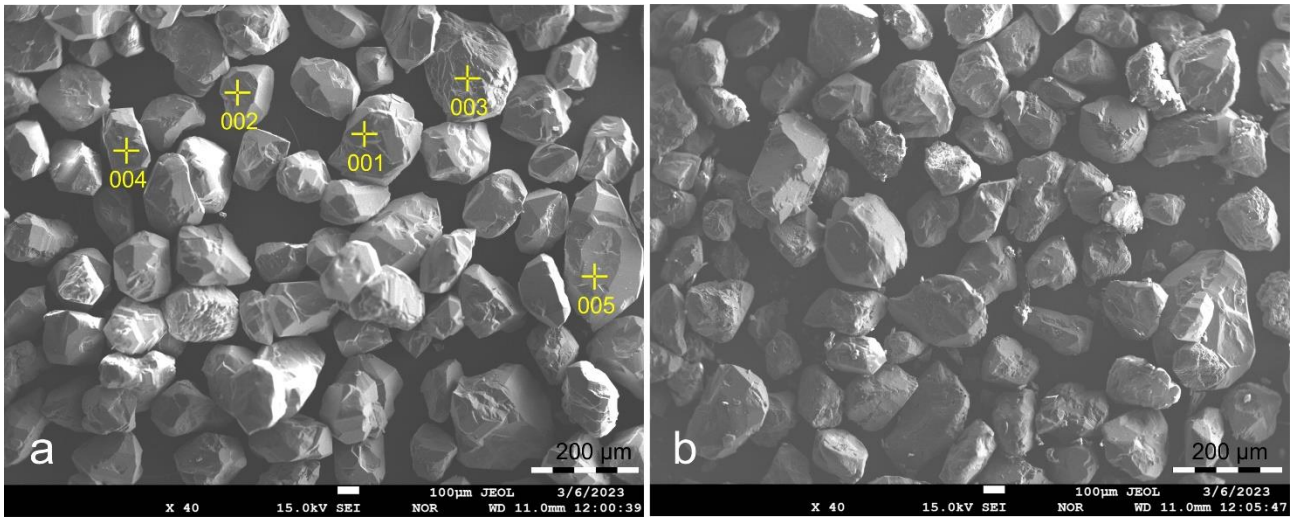

Figure 4.3. SEM images of quartz grains from the original Fontainebleau sandstone (a) and quartz grains from the post-test sample (b).

4.2.3 Procedure for the Determination of Silica Solubilities

For the solubility experiments, the sample cores were saturated with 2.5 wt% NaCl solution under vacuum before being placed in the reaction chamber. Then the flow-through system was saturated by careful flooding at low pressure (10—20 bar) over a period of four days until the electrical conductivity of the measuring cell had assumed a constant value. Then the final pressure was set before the temperature was increased. The experiments were carried out

at temperatures between 100 and 495°C and a constant pressure of 360 and 310 bar respectively, which guaranteed a single-phase fluid above the critical temperature, which is at about 286 bar and 403°C for the test fluid used.

As the set-up is equipped with electrodes, conductivity measurements were used to monitor fluid conductivities. This enables *in situ* detection when steady state conditions have been achieved in the reaction chamber, independent of flow rate.

Table 4.2. Applied flow rates and the resulting fluid-solid exposure times in the reaction chamber as well as the time needed to extract the fluid from the set-up.

Flow rate (mL/min)	Residence time (min)	Time until sample collection (h)
0.005	400	33.3 - 40
0.01	195	16.7- 20
0.015	133	11.1 – 13.3
0.02	98	8.3 - 10
0.03	65	5.6 - 6.7
0.04	49	4.2 - 5
0.05	39	3.3 - 4

Flow rates were varied between 0.00 and 0.05 mL/min. These low flow rates ensured effective preheating of the liquid and constant temperatures in the reaction chamber. It was observed that the cell conductivity was constant for fluid flow rates ranging between 0.00 and 0.03 mL/min, whereas for higher flow rates cell conductivities deviated considerably and the temperature increase became significant. In Table 4.2 the applied flow rates and corresponding residence times of the fluid volume in the reaction chamber are listed. Below the critical temperature (403°C, 286 bar), a flow rate of 0.01 mL/min was set, assuming that this would contribute to a rapid attainment of equilibrium conditions. Above the critical point, the flow rate was slightly increased to 0.015 mL/min to speed up sampling. In the course of the study, it became apparent that the flow rate specified on the injection pump was subject to drift. Therefore all flow rates were checked by balancing the volumes collected on the downstream side and corrected if necessary.

The total silicon concentration in the fluid samples was determined by ICP-OES. In addition, aliquots of most of the liquid samples were analysed photometrically for the monomeric silicon content immediately after sampling from the media separator. It was tested with the Silicomolybdenum blue method using a WTW S12 photometer.

4.2.4 Procedure for Kinetic Experiments

The original plan was to use electrical impedance spectroscopy as an *in situ* method to monitor the formation of mineral precipitates from electrolytic solutions. The precipitation rates of amorphous silica from a supersaturated solution were to be investigated by time-lapse spectroscopy under different temperature and pressure conditions. Complex conductivities (σ^*) or complex resistivities ($1/\sigma^*$) respectively, are used in geoelectrical applications to investigate charge transfer and polarisation behaviour under an external current to identify characteristic features indicating conduction pathways or barriers in the liquid-solid system. Recent studies have illustrated the importance of time-lapse complex conductivity measurements for the understanding of reaction mechanisms during precipitation at low temperature (Wu et al., 2010). Figure 4.4 displays a first test measurement and depicts frequency spectra measured in a stagnating silica-rich fluid at constant pressure and temperature conditions.

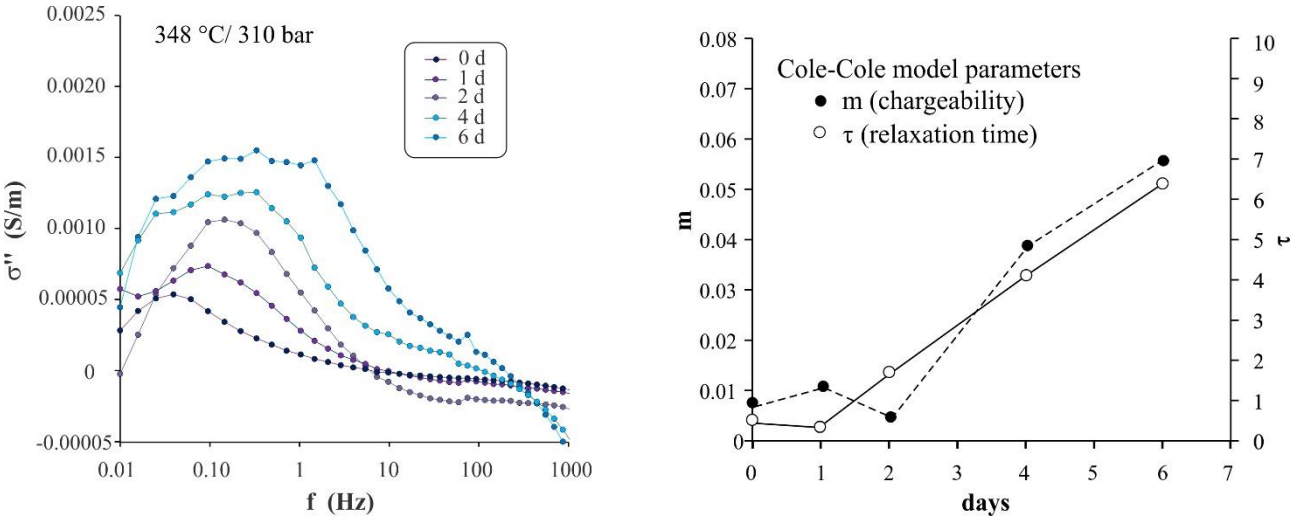

Figure 4.4. (a) Development of frequency spectra of imaginary conductivities measured in a stagnating silica-rich fluid at constant pressure and temperature conditions. (b) Cole-Cole model parameters, derived from the frequency spectra.

Conductivity in an alternating electric field is a complex quantity consisting of a real part of the complex conductivity and an imaginary part, where the imaginary conductivity depends only on processes at solid-liquid interfaces, while the real part of the conductivity represents both electrolytic conductivity and interface effects. Test measurements have shown that stopping the liquid flow leads to significant changes in the complex conductivity and to remarkable polarisation signatures in the low frequency range. When plotted against

frequency, the imaginary part of the conductivity shows a shift in amplitude and position of the peak with time, indicating a change in relaxation time, which is related to the length scale of induced charge separation along the fluid-solid interface (Bingley et al., 2005). Therefore, the initial approach was to use time-lapse measurements under stagnant conditions to record a consistent pattern of amplitudes shifting with time and possibly identify a common feature of polarisation signatures. In combination with ICP-OES analyses and photometer measurements of fluid samples, it should have allowed us to link the signature to ion complexation and a certain amount of precipitated minerals respectively.

The test involved heating the reaction chamber to 375°C to achieve maximum silica saturation in the test fluid and then reducing the temperature to 350°C to initiate silica precipitation from a now supersaturated solution. Crystallisation nuclei were already present in the reaction chamber in the form of the quartz grains from the sandstone cores. However after only 6 days we temporarily lost the temperature signal and after 18 days we lost control of the fluid, indicating a severe plugging of the capillary system. Therefore the experiment had to be terminated prematurely. The damage to the flow cell included an electrode sintered into the ceramic liner on the downstream side as well as a considerable amount of scalings clogging filters and valves (Figure 4.5).

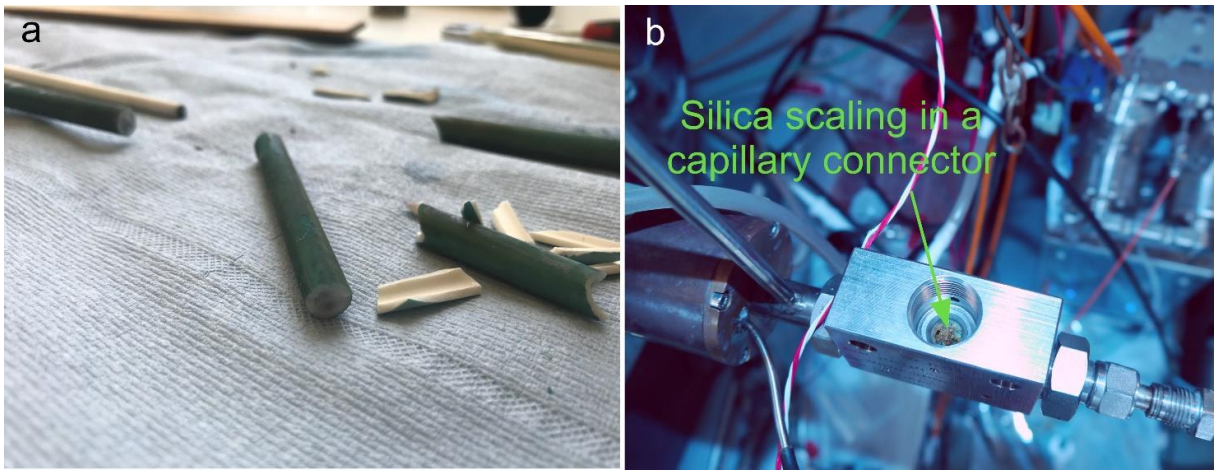

Figure 4.5. (Left) The photo shows fragments of the ceramic liner of the flow-through cell. The annulus is completely sealed with amorphous silica, so that one of the electrodes and the liner are tightly sintered together. (Right) View into a capillary connector clogged by silica precipitations.

The cost-intensive repair of the system took several weeks. Therefore the remaining experiments were carried out under dynamic conditions and in accordance with the experimental approach at IFE (Task 1.3.2) variable flow rates were used. However in contrast to IFE here only small flow rates below 0.1 mL/ min could be applied to avoid turbulences in the narrow annulus of the used flow-through cell. It was assumed that at a flow rate of 0.01 mL/min and a residence time of the fluid in the reaction chamber of more than 3 hours, the fluid-rock system has enough time to reach an equilibrium with maximum silica saturation, where the dissolution rate is zero. In contrast, increasing flow rates prevent equilibrium from

being reached in the reaction chamber, resulting in a test fluid increasingly undersaturated in silica.

4.3 Results and Discussion

4.3.1 Silica Solubility in High-Enthalpy Fluids

It is well known that the solubility of quartz in aqueous solutions increases nearly exponentially with temperature up to a maximum, which is slightly below the critical point and then decreases again steeply. In the present study, the maximum is expected at about 365°C (see personally communicated model by Morton Tjelta in Figure 4.6).

In the present tests between 200 - 350°C a huge discrepancy in measured and modeled silica solubilities by more than 50% is observed and no equilibrium silica concentration was reached during an experimental runtime of 22 days. In this temperature range, a nominal flow rate of 0.01 mL/min was applied, which was regarded as low enough to ensure equilibrium conditions. In contrast, at 400°C, 410°C and 435°C the model and experimental data are in excellent agreement with a slightly higher flow rate of 0.015 mL/ min and the tests running for 7 days at maximum. Only at 495°C does the solubility fall significantly below the model curves.

Figure 4.7 shows that the silica concentration in the liquid samples initially increases with the flow rate up to a threshold value of 0.015 mL/min. This could be due to the special design of the flow-through system, where the test liquid from the reaction chamber has to pass the downstream capillary system with a dead volume of 10 cm^3 before being collected in the media separator. Depending on the flow rate, this delays sampling by several hours to days (see Table 4.2). It would therefore be possible that at flow rates tending towards zero, precipitation of silica could already occur on the way to the media separator, with scalings being retained in the fluid filter.

The flow rate also seems to have an influence on the ratio of monomeric silica to total silica. The ratio was found to be nearly 1 for the test series at 0.015 mL/min, meaning that all silica was present in its monomeric species when the sample was taken (Figure 4.8). In contrast, for the test series at nominal flow rate of 0.01 mL/min a significant portion of the dissolved silica is already dimerized or polymerized when the samples were taken. Correspondingly, the monomer content reduces significantly, especially at higher temperature.

In addition to the flow rate, the supercritical state above a temperature of 405°C could also be a reason for the better agreement between the measured data and the solubility model, which could point to accelerated dissolution kinetics of the high-enthalpy system.

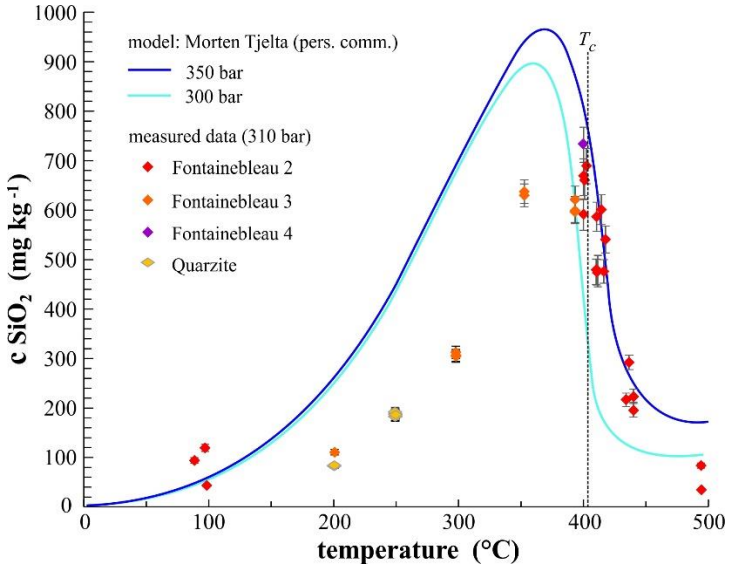

Figure 4.6. Temperature dependence of silica solubility in a 2.5 wt% NaCl test fluid. Symbols display measured data, solid lines represent solubility models of Morton Tjelta. T_c is the critical temperature.

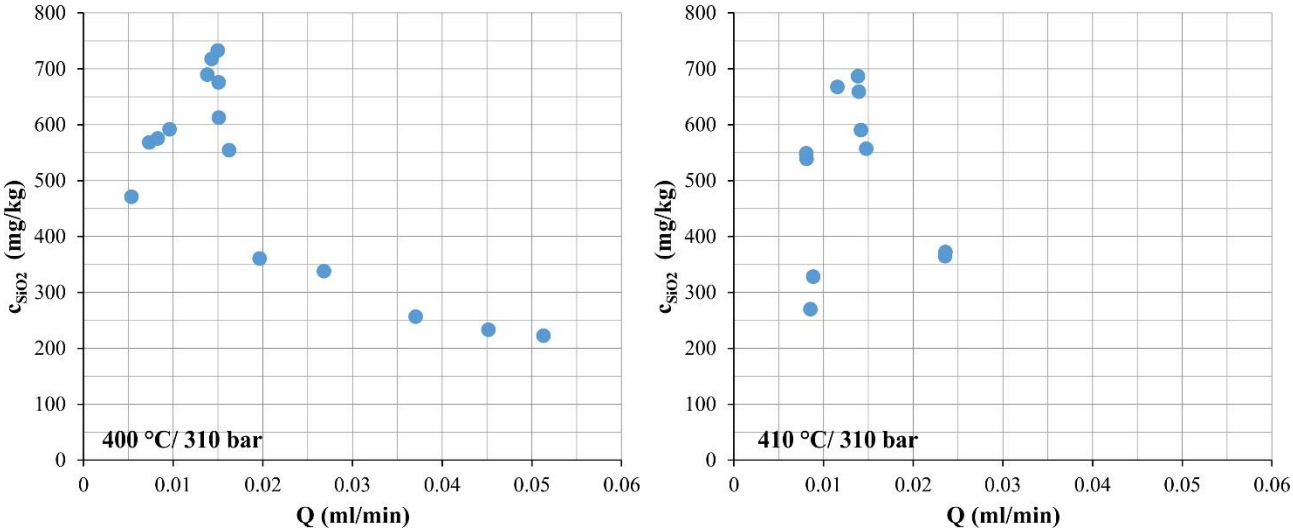

Figure 4.7. Silica solubility in a 2.5 wt% NaCl test fluid in dependence of flow rate. T = 400°C and p = 310 bar.

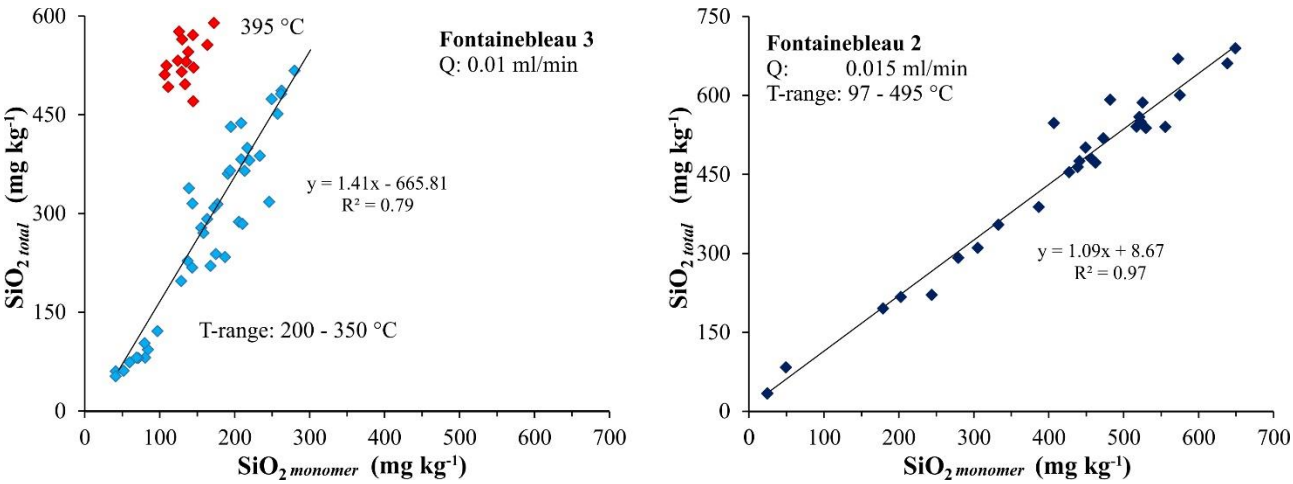

Figure 4.8. Total silica concentration plotted versus monomeric silica concentration for two solubility tests with Fontainebleau sandstone at a flow rate of 0.015 mL/min (left) and of 0.01 mL/min (right) and temperatures ranging from 200 to 395°C and 97 to 495 °C, respectively.

4.3.2 Kinetics of Quartz Solubility in High-Enthalpy Fluids

Due to experimental drawbacks on the one hand (see section 3.2.2) and a pandemic-related lack of time on the other, only one kinetic experiment was carried out at 400°C (near-critical conditions). ICP-OES data are still pending and are expected by the end of October 2023. Therefore, results cannot be included into this report.

4.4 Concluding Remarks

During the course of the study, some insights have emerged regarding the performance of reactive experiments under high temperatures and pressures: Although kinetic experiments in flow cells are quite common (see IFE report), the facility available at the GFZ is only suitable to a limited extent.

(1) The amount of sample material is small.

(2) Due to the built-in electrodes, the fluid can only flow through a narrow annulus, which poses the risk of clogging, especially in a reactive system with a high load of dissolved chemical components. In particular, the system proved unsuitable for tests under static conditions.

(3) Due to the length of the flow-through apparatus, hours to days elapse between fluid-solid interaction and sample collection, depending on the flow rate. For flow rate tending to zero, this may potentially lead to errors in the analysed silica concentrations.

Nevertheless, the accompanying conductometric monitoring during the solubility experiments has proven to be useful, as it makes it possible to detect *in situ* when steady state conditions are achieved, which simplifies the sampling. In addition, it was shown that spectrometric impedance measurements are generally possible under high-pressure, high-temperature conditions. Even though the flow-through apparatus used at GFZ is unsuitable for kinetic precipitation experiments due to the above-mentioned design and therefore no

systematic study could be carried out within the framework of the project, frequency spectra were recorded in a test run, indicating the potential of this method to monitor ion complexation and/or precipitation processes. For this, the 9/16" pressure tube could be substituted by a 60 mm pressure vessel, which would allow – besides a larger amount of sample material – an electrode arrangement where the fluid flow would be only marginally impeded.

4.5 References

Atkinson, G., Oklahoma, U., Raju, K., Aramco, S., Howell, R.D., 1991. The thermodynamics of scale prediction, SPE International Symposium on Oilfield Chemistry, Anaheim, California, February 1991, SPE-21021-MS, 209-215.

Baba, A., Özcan, H. and Deniz, O., 2005, April. Environmental impact by spill of geothermal fluids at the geothermal field of Tuzla, Canakkale-Turkey. Proceedings World Geothermal Congress (pp. 1-8).

Bingley, A., Slater, L.D., Fukes, M., Cassiani, G., 2005. Relationship between spectral induced polarization and hydraulic properties of saturated and unsaturated sandstone. Water Resources Res., 41, W12417, DOI: 10.1029/2005WR004202.

Dixit, C., Bernard, et al., 2016. Experimental study on the kinetics of silica polymerisation during cooling of the Bouillante geothermal fluid (Guadeloupe, French West Indies). Chemical Geology, 442, pp.97-112.

Dixit, C., Bernard, Mischer-Zita, M., 2019. Silica precipitation from geothermal fluid and synthetic solutions: Salts effects on kinetics and mechanism. European Geothermal Congress 2019, Den Haag, The Netherlands, 11.-14. July 2019.

Gunnarsson, I., Arnorsson, S., 2005. Impact of silica scaling on the efficiency of heat extraction from high temperature geothermal fluids: Geothermics, 34, pp.320-329.

Köhl, B., Grundy, J., Baumann, T., (2020). Rippled Scales in a Geothermal Facility in the Bavarian Molasse Basin: A Key to Understand the Calcite Scaling Process. Geotherm. Energy, 8, 1–27.

Sigfusson, B., Gunnarsson, I. 2011. Scaling prevention experiments in the Hellisheiði power plant, Iceland. Proceedings, thirty-sixth workshop on geothermal reservoir engineering, Stanford University, Stanford, California, SGP-TR-191.

Van den Heuvel, D.B., Gunnlaugssonb, E., Gunnarssonb, I., Stawskia, T.M.; Peacocka, C.L., Benning, L.G., 2018. Understanding amorphous silica scaling under well-constrained conditions inside geothermal pipelines. Geothermics, 76, 231-241, DOI: 10.1016/j.geothermics.2018.07.006

Wanner, C., Eichinger, F., Jahrfeld, T., and Diamond, L.W., 2017. Causes of abundant calcite scaling in geothermal wells in the Bavarian Molasse Basin, Southern Germany, Geothermics, 70, 324-338.

5 Kinetics of Silica Polymerisation in Metal Silicate Solutions informed by the Tuzla Geothermal Study Area

Mustafa Demir
İzmir Institute of Technology, Türkiye

5.1 Introduction

Silicate scaling has been heavily observed in Tuzla, which is the plant to be studied in Reflect. Both amorphous and metal silicate scaling has been observed in the plant. Tuzla geothermal power plant is in the northwestern part of Türkiye, 5 km from the Aegean Coast and 80 km south of Çanakkale (Figure 5.1). The brine and steam components of the two-phase geothermal fluid produced by artesian flow from two production wells are separated at the well-head in horizontal separators, and the brine is transferred to the ORC (Organic Rankine Cycle) plant by booster pumps. In this report, structural characterization of the deposit obtained from Tuzla region is carried out using microscopy and spectroscopy. Artificial metal silicate powder has been produced for understanding the interaction of silica network and metal ions. Lastly, kinetics of polymerisation is investigated including the order of reaction, rate constant, and activation energy using Arrhenius type of equation.

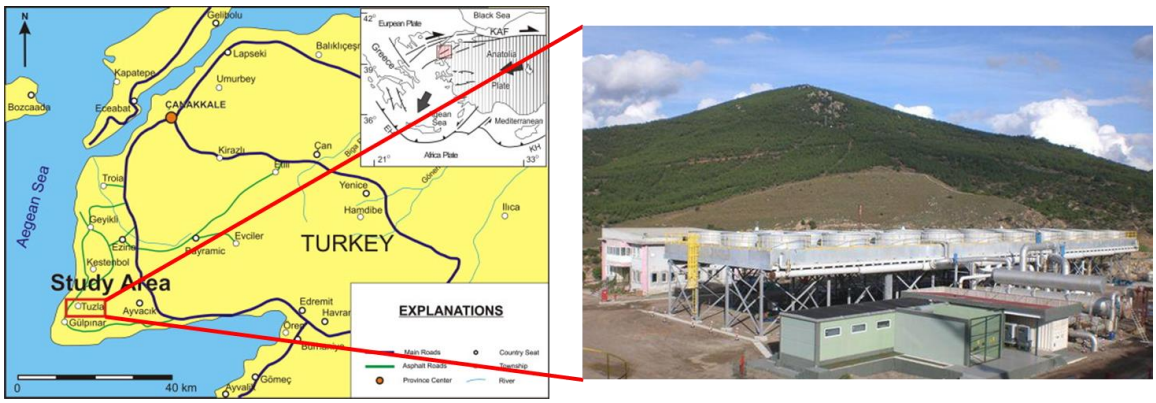

Figure 5.1. Tuzla Geothermal Power Plant located in Çanakkale, Ayvacık (Türkiye).

5.2 Characterisation of Natural Metal Silicate

The deposit obtained from Tuzla regions has been characterised periodically. The power plant experienced two stoppages in a year. Deposit samples were collected and examined by Scanning Electron Microscopy (SEM) and X-ray Fluorescence spectroscopy (XRF). The results were reported in literature (Demir et al., 2014). In the Reflect project, we further perform characterization using Transmission Electron Microscopy and X-ray Photoelectron Spectroscopy (XPS).

Figure 5.2 presents two representative TEM images of the natural deposit obtained from two different regions. In the first image, the scale bar is 10 nm. Fibrillary morphology is evident, which suggests the existence of (metal) silicates.(Casar et al., 2023) Elemental analysis from the Energy Dispersive X-ray Spectroscopy (EDX, right-hand side) suggests the existence of Si and Fe ions in the structure. The second image shows bright spots in the metal silicate matrix.

In electron microscopy, bright colour refers to the structures containing heavy atoms compared to the surrounding matrix. Elemental analysis on these domains clearly displays the formation of iron oxide in the deposit. The existence of two different structures (both silicate and oxide) suggests that the deposit is heterogeneous in nature in terms of both morphology and chemistry.

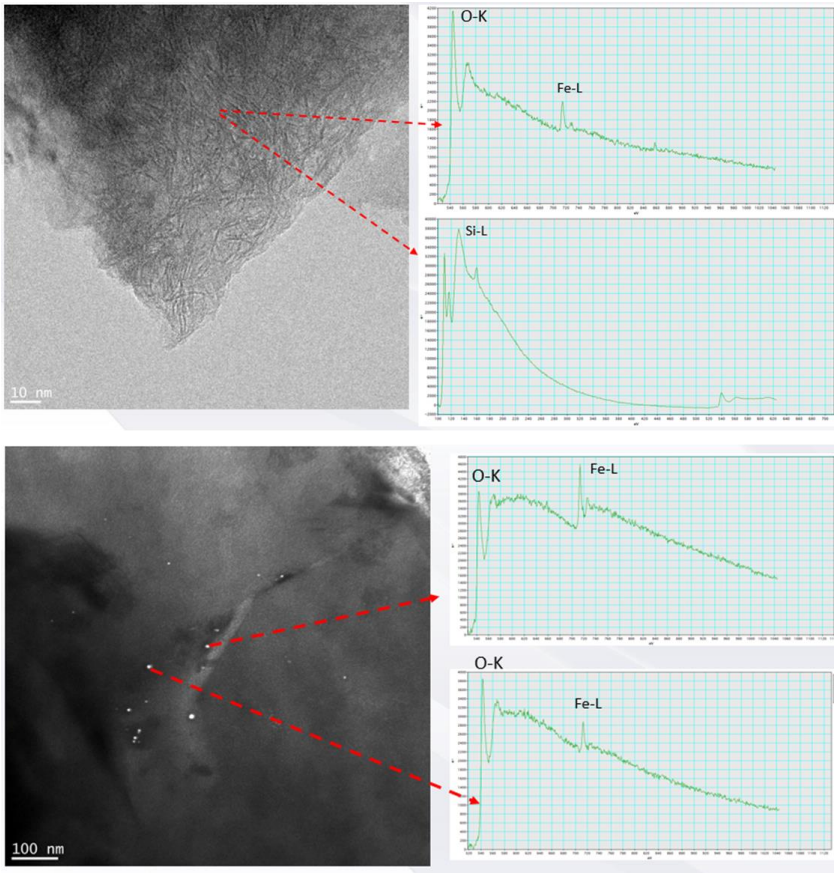

Figure 5.2. TEM images and EDX of natural Fe,Mg silicate deposit.

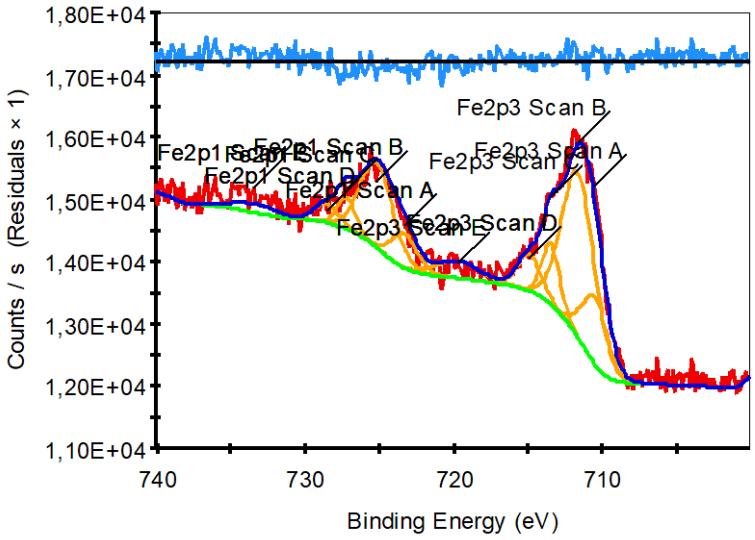

Figure 5.3. XPS of the natural deposit obtained from Tuzla.

Iron has two different valence states suggesting the formation different structures as inferred from examination using XPS. Figure 5.3 displays a representative XPS result of the natural deposit focusing on the valence of iron. Four different signals were detected, which are listed in the first column in Table 5.1 where the second column shows the potential origin of the signals. Two of them are strong signals, the other two of them are weaker satellites that is typically present in spectroscopy. Signals that appeared at 712 and 726 eV may originate from $Fe2p_{3/2}(Fe_2O_3)$ and $Fe2p_{1/2}(Fe_2O_3)$, respectively. The signals were deconvoluted (orange line), showing the existence of heterogeneous structures in the deposit.

Table 5.1. XPS signals of the natural deposit obtained from Tuzla.

Energy (eV)	XPS signal
712	$Fe2p_{3/2}(Fe_2O_3)$
720	$Fe(III)Fe2p_{1/2}$ (Satellite)
726	$Fe2p_{1/2}(Fe_2O_3)$
734	$Fe(III)Fe2p_{3/2}$ (Satellite)

5.3 Bulk Precipitation of Metal Silicate (Stöber Method)

To get insight on the effect of metal ions on silica polymerisation, silica is obtained in the lab using Stöber synthesis method under various conditions. Using tetraethyl orthosilicate as starting material, silica polymerisation is obtained in alkali solution (NH_3) and precipitated as colourless powder by centrifugation. Figure 5.4 shows X-ray Diffractogram (XRD) of the powder obtained at different temperatures (25°C, 40°C, or 80°C) and time (40 min or 80 min). Red line refers to the XRD of silica powder without metal ions. The diffractograms show amorphous halo, i.e. no crystallinity. The addition of metal ions, except Na^+, did not affect the

diffraction character of the powder. However, the reaction taking place in the presence of Na^+ causes the appearance of new reflections in the diffractogram, indicating formation of secondary phases consisting of various complex structures.

The morphology of the silica particles is examined by SEM images given in Figure 5.5. Silica particles without metal ions have spherical uniform morphology. In the presence of metal ions, the spherical morphology is distorted. In the presence of Na^+, additional structures are observed. This result may be in line with the formation of new phases observed in diffractogram of the silica powder synthesized in the presence of Na^+.

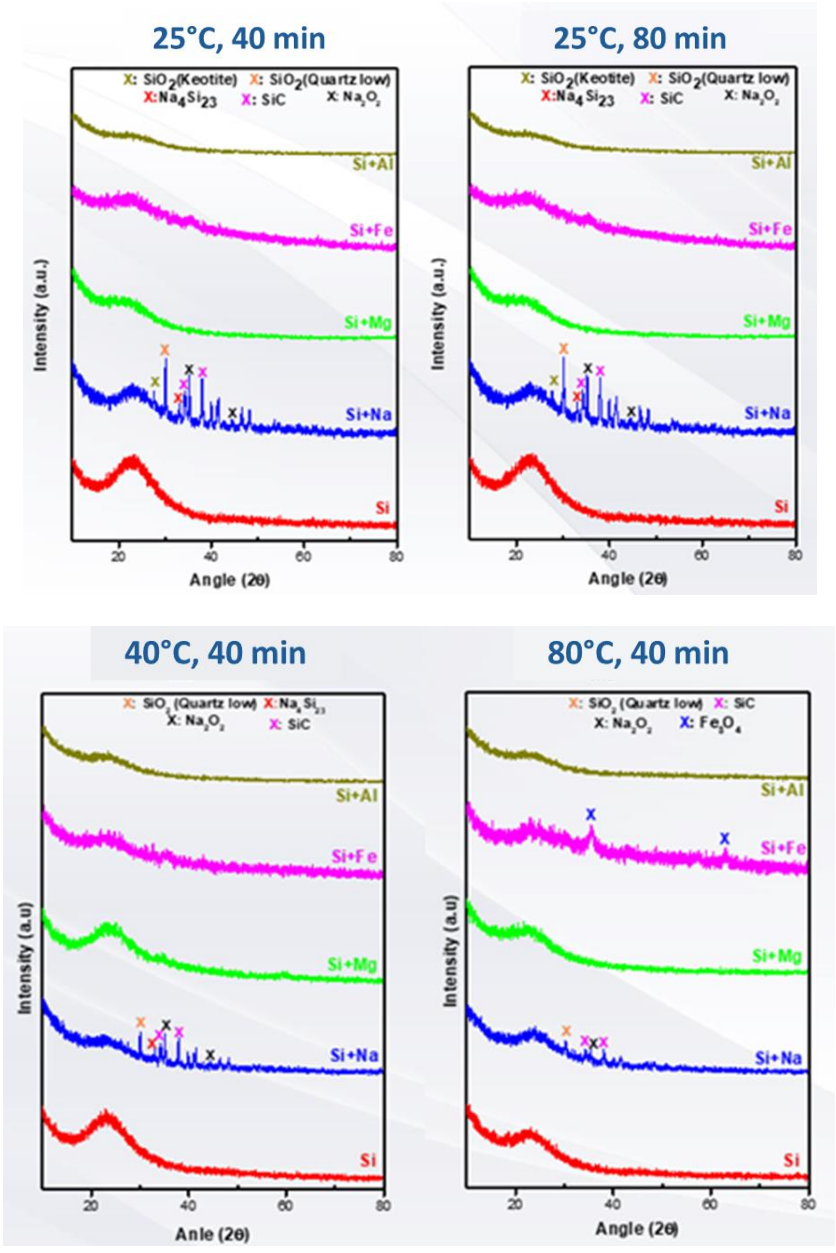

Figure 5.4. XRD pattern of the silica particles prepared in the presence of metal ions.

	25°C, 40 min	40°C, 40 min	80°C, 40 min
Si	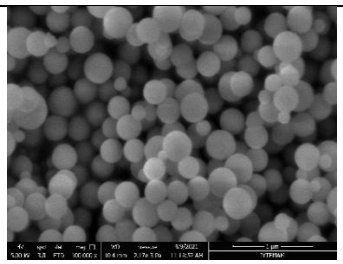	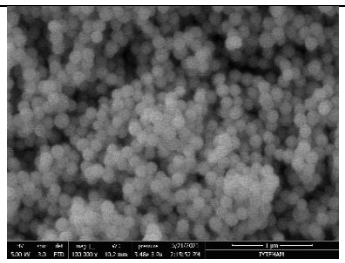	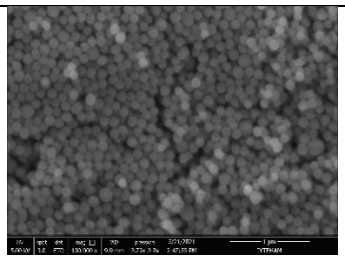
Si+Fe	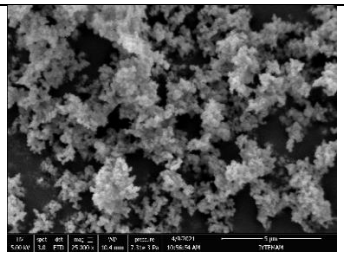	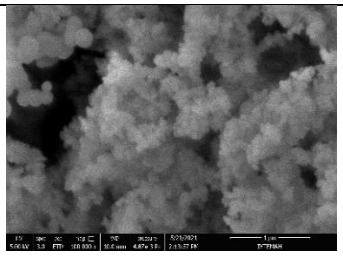	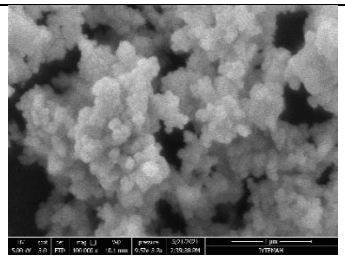
Si+Mg	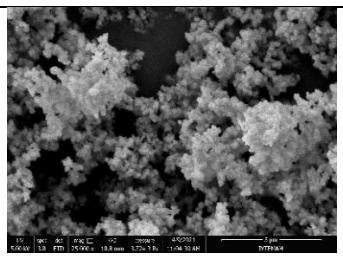	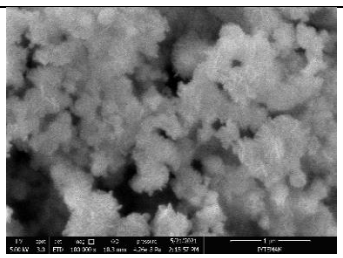	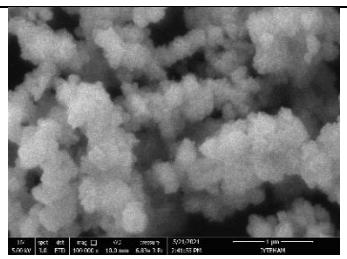
Si+Al	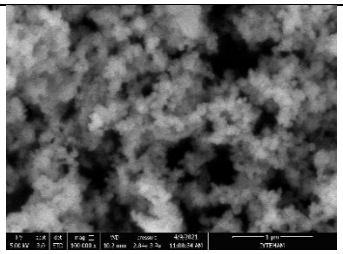	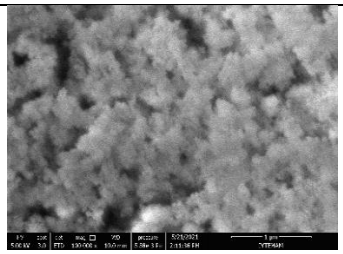	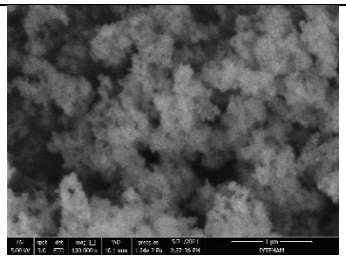
Si+Na	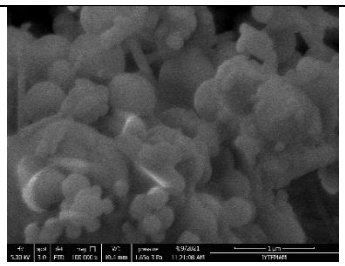	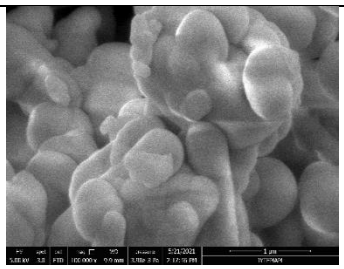	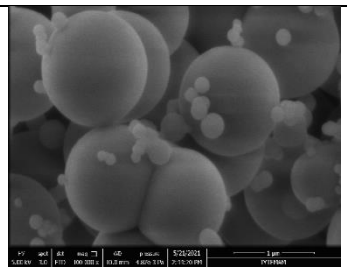

Figure 5.5. SEM images of the silica particles prepared by Stöber method at ×5,000 magnifications.

The critical question regarding the metal silicate could be the integration of metal ions to the silica network. The silica particles prepared in the presence of metal ions are studied by TEM. Figure 5.6 presents a representative high resolution of TEM image of silica particles prepared in the presence iron ion. Lattice fringes are evident in the image. Lattice spacing of the fringes have 0.25 nm, 0.26 nm, and 0.27 nm that may refer to the existence of Fe_3O_4 Magnetite (311, 011), Fe_2O_3 (104), Fe_3O_4 (101), respectively. Figure 5.6b presents the chemical analysis drawn on a red line in the image. The analysis shows the existence of Si and Fe on the line. When the red line crosses bright domains, iron signal is high and silica signal is low. This result suggests that iron ions does not participate in the silica network, but rather forms small iron oxide domains in the silica network.

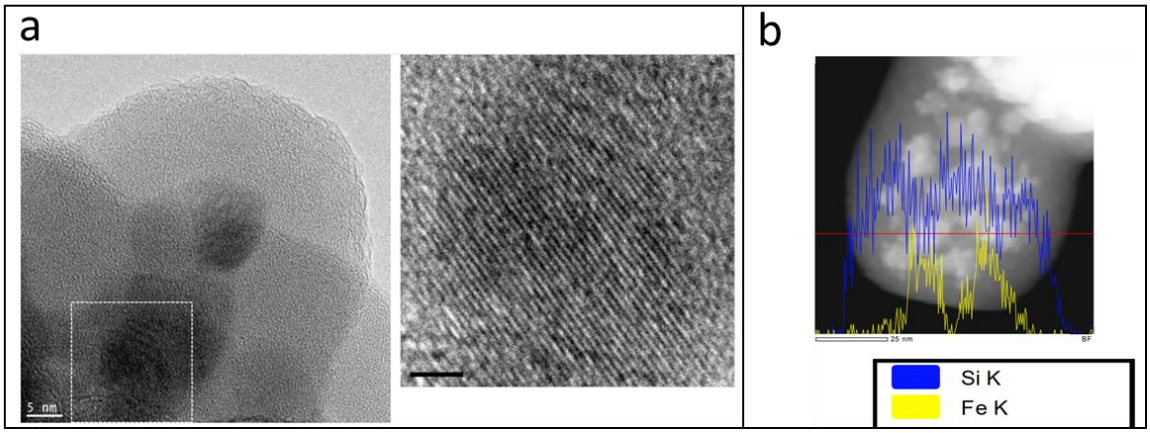

Figure 5.6. a) A representative TEM image of the domains in silica network b) Chemical mapping on red line by EDX.

Vibration spectroscopy was employed for the validation of this hypothesis. If a metal ion participate to the silica network, the vibrational bands should be shifted. Figure 5.7 presents Fourier Transform Infrared Spectroscopy results of the silica network prepared in the presence of metal ions. None of the vibrational bands undergoes shifting suggesting that metal ions form an additional phase in the silica matrix.

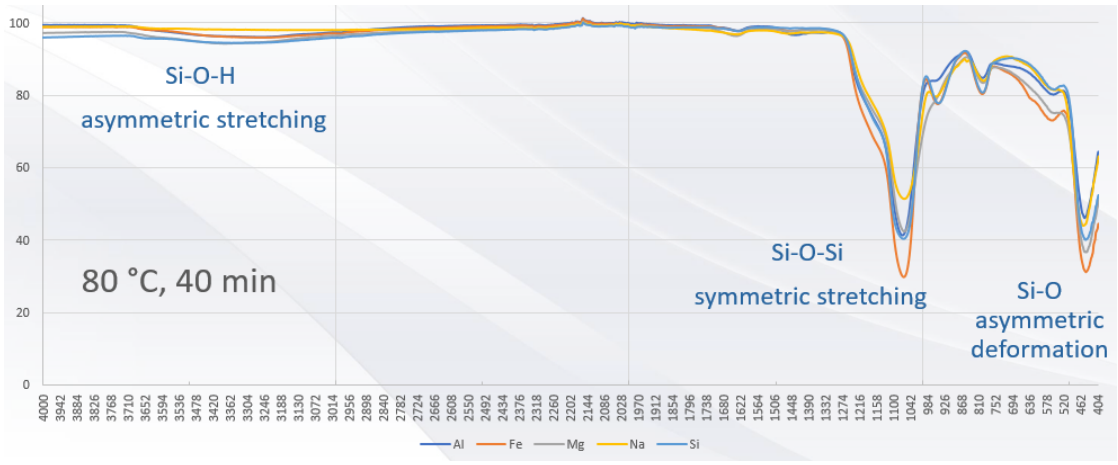

Figure 5.7. Vibrational spectra of the silica particles prepared in absence/presence of the metal ions.

5.4 Kinetics of Silica Polymerisation

Silica precipitation takes place at every part of the power plant starting from the injection well to the reinjection one. To understand the formation mechanism, kinetics of polymerisation is studied varying the parameters such as temperature, pH, and chemistry of metal ions (0.01 M). Order, rate, and activation energy of the polymerisation are estimated based on the results obtained from synthetic brine. The polymerisation path of aqueous silica species is represented in Figure 5.8.

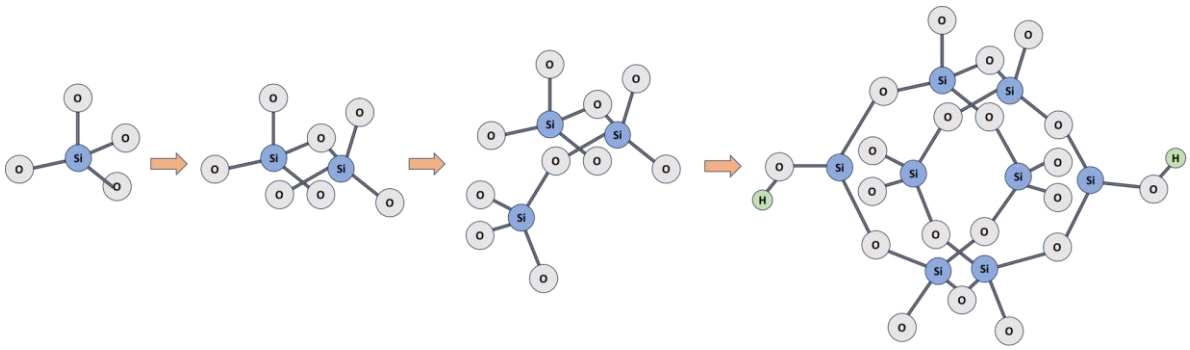

Figure 5.8. The mechanism of silica polymerisation

5.4.1 Preparation of the Particles

Synthetic silica solution was prepared from 1000 ppm SiO_2 diluting $Na_2SiO_2 \cdot 2H_2O$ solution in 250 mL of deionized water. An aliquot of 500 µL ammonium molybdate and 500 µL sulfuric acid were added to obtain the yellow colour (Figure 5.9). 100 g/L ammonium molybdate solution was prepared by dissolving 5 g of ammonium heptamolybdate in 100 mL deionized water. For the preparation of 1.5 M of H_2SO_4, which was to make acidified media for the silicomolybdate in the experiments, 20,8 mL of 98% H_2SO_4 (18 M) was taken and added to 250 mL deionized water in a 500 mL volumetric flask, and then completed with deionized water up to 500 mL. For the 500 mL volumetric flask used to prepare the 1M of HCl for pH adjustment, 41.6 mL of 37% HCl (12 M) was taken and poured into 250 mL of deionized water first.

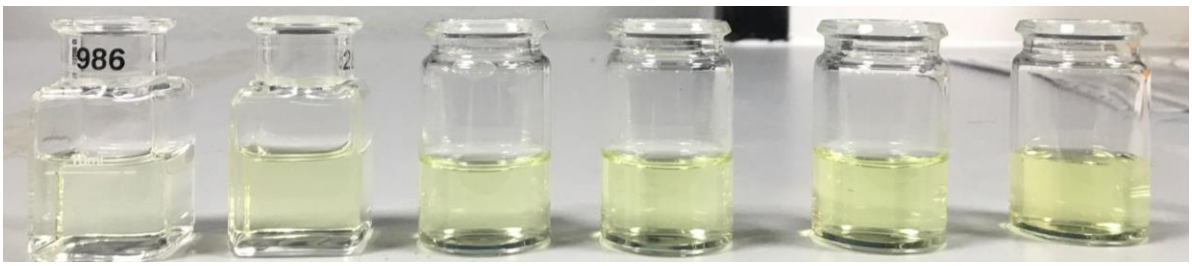

Figure 5.9. Silicomolybdic samples from 20 mg/L to 100 mg/L.

5.4.2 Effect of Temperature

The effect of temperature was studied at the temperature of 25°C (298 K), 45°C (318 K), and 90°C (363 K). The results are shown in Figure 5.10. The concentration of monomeric silica rapidly drops over time at all temperatures and shows exponential decay till the silica solubility at the temperature of interest. The monomeric silica concentration approaches the solubility level for all temperatures in 6 h. Dixit et al. (2016) stated that this continued decrease lasted for about 3 days in the 25°C experiment. The experiment at 25°C shows the rapid decrease of monomeric silica concentration.

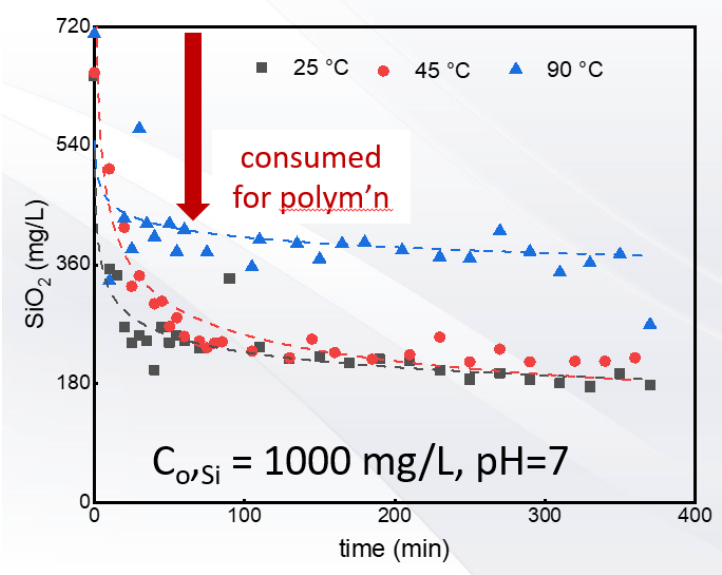

Figure 5.10. Silica concentration as a function of time at various temperature.

5.4.3 Effect of pH

The concentration of molybdate active silica initially contained about 650 mg/L SiO_2. It has been used for the 6 h of polymerisation. For the pH range employed in this study, pH 5 to 8, the rate of silica polymerisation shows remarkable variation. In the initial stages of the experiment, monomeric silica concentrations are relatively stable for some time before starting to decrease. At relatively low pH, polymerisation was found to be slow, and it is considered an induction period in literature. This time is estimated to be the formation of the critical size of the polymeric silica network (Icopini et al., 2005). After the induction period, the monomeric silica concentration at pH 5 decreases very slowly, and after 9 h, no equilibrium has been reached. However, the monomeric silica concentration at pH 7 and 8 rapidly decreases without an induction period. Results shown in Figure 5.11 support this hypothesis.

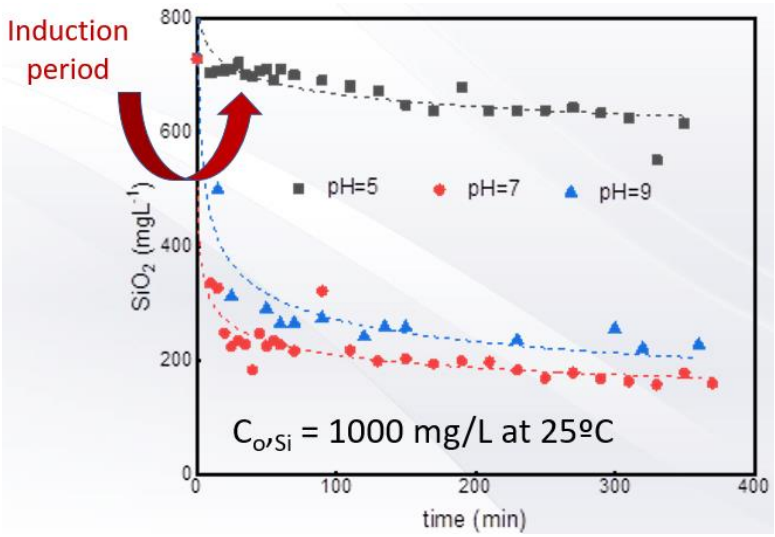

Figure 5.11. Silica concentration as a function of time at various pH.

5.4.4 Effect of Metal Ions

The effect of metal ions is examined keeping the reaction conditions fixed (0.01 M, at 25°C, and pH=7) in order to understand the potential impact of the presence of the metal ions on the silica polymerisation. Figure 5.12 shows the concentration of monomeric silica concerning reaction time attained with the same concentration of the metal ions (Fe^{3+}, Al^{3+}, Mg^{2+}, Na^{+}) at 0.01 M. Similarly, the concentration of silica shows an exponential decay with a sharp initial decrease of the concentration before levelling off to the solubility of silica in the presence of the metal ions. Initially, silica is rapidly consumed and then the consumption rate is reduced suggesting that there are not enough silica molecules to keep this rate, i.e. the concentration of the silica is not high enough for polymerisation. Similar to this mechanism, the results obtained in the presence of metal ions show a similar decrease in silica concentration. The maximum consumption is seen in the presence of Fe^{3+}. The consumption rate is higher than the one of blank, i.e., polymerisation without Fe^{3+}. This result may suggest that consumption is heavily seen since Fe^{3+} may be reactive in polymerisation. One can speculate that Fe(silicate) may be the initial compound in the formation of the geothermal deposit in the actual geothermal field. Mg^{2+} and Al^{3+} also show similar effects on polymerisation, triggering the appearance of corresponding metal silicates. Apart from these three ions, Na^{+} shows the opposite behaviour. The existence of Na^{+} reduces the rate of consumption of monomeric silica. It may be one of the reasons that Na^{+} is not present in the deposit of the Tuzla geothermal field.

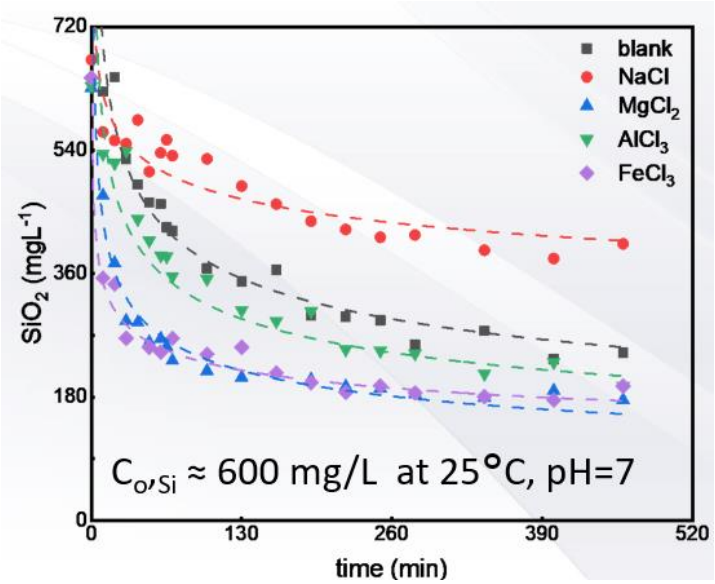

Figure 5.12. Silica concentration as a function of time at various metal ions. The concentration of metal ions is 0.01 M.

The effect of metal ions on silica polymerisation was investigated by adding the ions separately and mixing, keeping the rest of the reaction parameters unchanged. Each metal salt was added to 600 mg/L silica solution equimolar (2.5 mM), and the experiment was repeated using the same procedure as described above. The results are presented in Figure 5.13. The silica concentration shows similar behaviour as a function of time. It has exponential decay at both temperatures. At 90°C, the solubility level is higher as expected compared to the reaction taking place at 25°C. The solubility level reaches a value of around 180 ppm, which is similar to the level eventually obtained when Fe^{3+} and Mg^{2+} ions are present individually in the polymerisation medium (Figure 5.12). This level is higher in the presence of Na^{+}. One can conclude that when Na^{+} and Fe^{3+} are both present in the reaction medium, Fe^{+3} dominates. This can be seen from the grey line in Figure 5.13 being more similar to the purple $FeCl_3$ line than the red NaCl line in Figure 5.12.

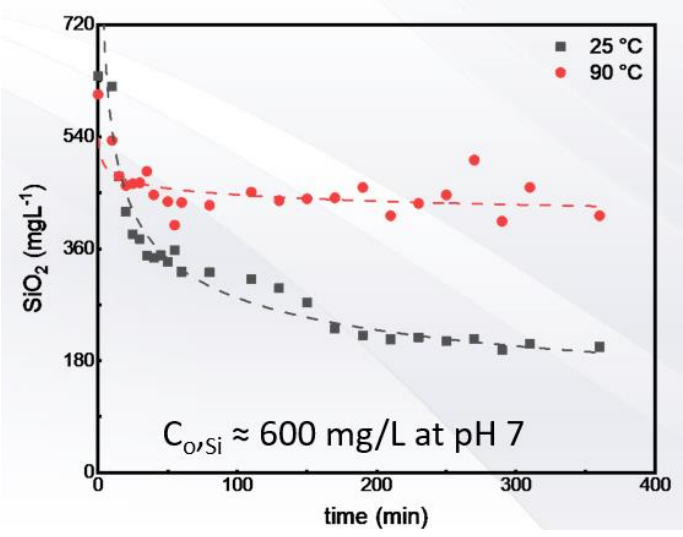

Figure 5.13. Silica concentration in the presence of metal ion mixture.

5.4.5 Rate Order and Activation Energy

Rate order and activation energy for the silica polymerisation in the absence and presence of metal ions is examined for synthetic brine. The rate of the experiments was calculated for 25°C at neutral pH. The rate of the experiment was estimated by Equation (1) and integrated into Arrhenius' Equation as shown in Equation (2)

$$\text{Rate} = k\,[A]^a\,[B]^b \qquad (1)$$

where k is the rate constant; *A* is the concentration (mol/L); *B* is the concentration (mol/L); *a* is the order of reaction concerning *A*; *b* is the reaction relating to *B*.

$$k = A\,e^{-Ea/RT} \qquad (2)$$

k is the rate constant; E_a is the activation energy (J/mol); *T* is the temperature in K; R is the gas constant (J/K·mol); A is the pre-exponential factor; *e* is the base of the natural logarithm.

Rate constants were calculated at 25°C with and without metal ions. The order of the reactions was tested from zeroth to fourth and their R^2 values calculated. The third order rate constant was found most suitable with 0.91, and 0.96 R^2 values (Table 5.2).

Table 5.2. Order and rate constant of silica polymerisation.

	Order	**Rate constant $(mol/L)^{-2}\ s^{-1}$**
Without metal ions	3	4×10^{-7}
With metal ions	3	2×10^{-6}

The activation energies from 25 to 45°C and 45 to 90°C for the overall experiment were determined as 35 ± 2.1 kJ/mol and 36.4 ± 1 kJ/mol, respectively. Comparing the literature, this study's result has lower activation energies. Dixit et al. (2016) found 52 kJ/mol for the Bouillante geothermal brine with an initial SiO_2 concentration of about 600 at neutral pH. Rothbaum and Rohde (1979) found that the activation energy between 5 and 90°C has a low value of 12.25 kJ/mol, while the activation energy between 90 and 180°C appears negative. After the induction period, they observed the maximum rate order for monomeric silica has fourth-order dependence between 5 and 90°C. Carroll et al. (1998) found the activation energy as 61 ± 1 kJ/mol for Wairakei geothermal brine between 80 and 120°C at about neutral pH. In addition, for higher temperature ranges (20°C to 500°C), the activation energy was observed between 30 to 150 kJ/mol. The reason for the differences between the literature and this study may be the initial solution concentrations and the experimental conditions, and the calculation methods.

5.5 Conclusions

The deposit obtained from Tuzla region is heterogeneous in nature of silicates and oxides. Metal ions seems to form an independent oxide phase in the silica network matrix. Silica polymerisation shows *exponential decay* as a function of time both in the absence and presence of metal ions. The polymerisation follows *3rd order* kinetics (*n*=3), which remains unchanged in the presence of metals. The effect of metal ions on polymerisation follows the trend: $Fe^{3+} > Mg^{2+} > Al^{3+} >$ blank $> Na^{+}$. Rate constant is *higher by up to a factor of 10* in the presence of the metal ions. E_a lies in between *35.0-36.4 kJ·mol^{-1}* for mere silica polymerisation.

5.6 References

Carroll, S., Mroczek, E., Alai, M., & Ebert, M. (1998). Amorphous silica precipitation (60 to 120°C): comparison of laboratory and field rates. *Geochimica et Cosmochimica Acta*, *62*(8). https://doi.org/10.1016/S0016-7037(98)00052-0

Casar, Z., Mohamed, A. K., Bowen, P., Scrivener, K. (2023). Atomic-level and Surface Structure of Calcium Silicate Hydrate Nanofoils. J. Phys. Chem. C, 127, 37, 18652-18661. https://doi.org/10.1021/acs.jpcc.3c03350

Demir, M. M., Baba, A., Atilla, V., & Inanli, M. (2014). Types of the scaling in hyper saline geothermal system in northwest Turkey. *Geothermics*, *50*. https://doi.org/10.1016/j.geothermics.2013.08.003

Dixit, C., Bernard, M. L., Sanjuan, B., André, L., & Gaspard, S. (2016). Experimental study on the kinetics of silica polymerisation during cooling of the Bouillante geothermal fluid (Guadeloupe, French West Indies). *Chemical Geology*, *442*. https://doi.org/10.1016/j.chemgeo.2016.08.031

Icopini, G. A., Brantley, S. L., & Heaney, P. J. (2005). Kinetics of silica oligomerization and nanocolloid formation as a function of pH and ionic strength at 25°C. *Geochimica et Cosmochimica Acta*, *69*(2). https://doi.org/10.1016/j.gca.2004.06.038

Rothbaum, H. P., & Rohde, A. G. (1979). Kinetics of silica polymerisation and deposition from dilute solutions between 5 and 180°C. *Journal of Colloid And Interface Science*, *71*(3). https://doi.org/10.1016/0021-9797(79)90328-X

6 Conclusion of Deliverable 1.4

This report is a published product of the 'REFLECT' project – a Horizon Europe project which aims to inform the processes of geothermal energy extraction by determining the effect of relevant fluid properties and reactions in order to enhance predictive geochemical modelling and thus the energy exploitation and life-time of geothermal power plants.

The polymerisation and precipitation of dissolved silica is a significant obstacle to the efficient production of geothermal energy. The challenges associated with silica precipitation are well illustrated by the damage to experimental equipment reported in section 4.2.4. This report provides new data about the dissolution and precipitation of silica under conditions relevant to geothermal energy extraction.

Dissolution was studied under both sub- and supercritical conditions (100—495°C, 75—450 bar). Dissolution and/or precipitation behaviour of silica is described in contact with pure water (BGS), saline solution (IFE, GFZ) and metal silicate solutions informed by real geothermal samples from the Tuzla region of Türkiye (IZTECH).

In pure water it was found that the maximum dissolution of silica at a given pressure occured when the density of pure water was in the range 0.5 to 0.6 g/mL. In saline solution, measured dissolution rate constants are reported to be of the order 10^{-9} to 10^{-7} for liquid and supercritical water, and 10^{-12} to 10^{-11} in the vapour-like phase; precipitation rate constants were calculated to be 2 orders of magnitude larger for liquid and supercritical phases, and 3-4 times larger in the gaseous phase.

The presence of metal ions was found to have a variable effect of the polymerisation of silica, with certain species (Fe^{3+}, Mg^{2+} and Al^{3+}) increasing the rate constant by up to a factor of ten, but with sodium (Na^{+}) decreasing the rate. The process of polymerisation is found to follow third order kinetics, which remains unchanged in the presence of metal ions.

New methods of monitoring silica in solution were assessed in this report. A conductometric method was found to have potential for detecting and monitoring the processes of polymerisation and precipitation. Raman spectroscopy was shown to be capable of detecting silica in a bulk fluid, and also detected deprotonated monomers of silicic acid. Raman spectra also showed potential for the quantitative measurement of silica in solution.

The results presented in this report provide valuable insight into factors influencing silica scaling in geothermal systems. There remains scope for further research to provide a still more complete picture of the interactions of silica with geothermal waters across the full range of variables. Further work is also required to refine the monitoring methods studied for industrial application.